

1 **Supporting Information for “A quantitative comparison**
2 **and validation of finite-fault models: The 2011**
3 **Tohoku-Oki earthquake”**

4 **Jeremy Wing Ching Wong¹, Wenyan Fan¹, Alice-Agnes Gabriel^{1,2}**

5 ¹Scripps Institution of Oceanography, University of California San Diego, La Jolla, CA, USA

6 ²Department of Earth and Environmental Sciences, Ludwig-Maximilians-Universität München, Munich ,
7 Germany

8 **Supplementary Contents**

- 9 1. Text S1–S3
10 2. Table S1–S3
11 3. Figures S1–S43

Corresponding author: Jeremy Wing Ching Wong, [wchwong@ucsd.edu](mailto:wcwong@ucsd.edu)

Text S1: Overview of the 32 Finite-fault Slip Models

Model G1 is from Pollitz et al. (2011), which is obtained using geodetic measurements. The total moment of the model is 4.1×10^{22} N·m, equivalent to a M_w 9.01 earthquake. The model includes a total of 5151 subfaults, with 101 and 51 subfaults along the strike and dip directions, respectively. Each subfault has an area of 7×4.5 km². The model is parameterized as three planar faults with strike and dip as 195° and 10°, 195° and 14°, and 195° and 22° at the depth ranges of 3–21, 21–39, and 39–57 km. The rake angles of all subfaults are fixed at 90°. The model composes of two major slip patches located updip and downdip of the hypocenter in zones ZC1 and ZC2, with peak slip away from the trench.

Model G2 is from Ito et al. (2011), which is obtained using geodetic measurements. The total moment of the model is 4.1×10^{22} N·m, equivalent to a M_w 9.01 earthquake. The model includes a total of 525 subfaults, with 35 and 15 subfaults along the strike and dip directions, respectively. Each subfault has a varying area. The model is parameterized as a non-planar fault. The model composes of a single slip patch at the updip area in zone ZC1. The major slip patch is slightly south of the hypocenter, located between 37°N to 38°N.

Model G3 is from Diao et al. (2012), which is obtained using geodetic measurements. The total moment of the model is 2.3×10^{22} N·m, equivalent to a M_w 8.84 earthquake. The model includes a total of 288 subfaults, with 24 and 12 subfaults along the strike and dip directions, respectively. Each subfault has an area of 20×20 km². The model is parameterized as a non-planar fault. The model composes of a single smooth slip patch in zone ZC1.

Model G4 is from Iinuma et al. (2012), which is obtained using geodetic measurements. The total moment of the model is 4.0×10^{22} N·m, equivalent to a M_w 9.00 earthquake. The model includes a total of 806 subfaults, with 31 and 13 subfaults along the strike and dip directions, respectively. Each subfault is represented by bi-cubic B-spines with 20 km intervals. The model is parameterized as a non-planar fault. The model has the largest slip at the trench and extended along strike slip patch. The model consists of a secondary slip patch extending to the southern deeper region in zone S2.

Model G5 is from C. Wang et al. (2012), which is obtained using geodetic measurements and InSAR measurements. The total moment of the model is 3.2×10^{22} N·m, equivalent to a M_w 8.94 earthquake. The model includes a total of 1080 subfaults, with 60 and 18 subfaults along the strike and dip directions, respectively. Each subfault has an area of 11.7×11.1 km². The model is parameterized as a varying dip angle fault with a striking angle of 195°. The model has a single slip patch at the updip of the hypocenter in zone ZC1 with peak slip away from the trench.

Model G6 is from R. Wang et al. (2013), which is obtained from geodetic measurements and displacement from integrated strong ground motion waveforms. The total moment of the model is 2.9×10^{22} N·m, equivalent to a M_w 8.91 earthquake. The model includes 1920 subfaults with 64 subfaults along strike and 30 subfaults along dip. Each subfaults has a size of 10×10 km². The model is parameterized as a non-planar fault. The model composes of a single slip patch at the updip of the hypocenter in zone ZC1 with peak slip away from the trench.

Model G7 is from Zhou et al. (2014), which is obtained from probabilistic inversion of geodetic data. The total moment of the model is 3.8×10^{22} N·m, equivalent to a M_w 8.99 earthquake. The model includes 350 subfaults with 25 subfaults along the strike and 14 subfaults along the dip. Each subfault has a size of 25×18 km². The model is parameterized as a varying dipping angle fault with a striking angle of 201. The model has a horse-shoe-shaped slip patch surrounding the hypocenter with peak slip at the trench in zones ZC1 and ZC1.

63 Model G8 is from Hashima et al. (2016), which is obtained from geodetic measure-
 64 ments. The total moment of the model is 4.0×10^{22} N·m, equivalent to a M_w 9.00 earth-
 65 quake. The model includes 256 subfaults with 32 along-strike subfaults and eight along-
 66 dip subfaults. Each subfaults has a varying subfault area. The model is parameterized
 67 as a non-planar fault. The rake angles of all subfaults are fixed with the incoming plate
 68 direction. The model has a board and smooth slip patch with slip peaking at the trench
 69 at the updip area of the hypocenter in zone ZC1.

70 Model G9 is from Xie and Cai (2018), which applies stress inversion formulation
 71 for slip distribution from geodetic measurements. The total moment of the model is $4.5 \times$
 72 10^{22} N·m, equivalent to a M_w 9.04 earthquake. The model includes 140 subfaults with
 73 20 along-strike subfaults and seven along-dip subfaults. Each subfaults has a $25 \text{ km} \times 25 \text{ km}$
 74 subfault area. The model is parameterized as a non-planar fault. The model has a board
 75 and smooth slip patch with slip peaking at the trench in zone ZC1, with a slightly wider
 76 rupture than other geodetic models.

77 Model R1 is from Lee et al. (2011), which is obtained by inverting regional veloc-
 78 ity waveform integrated from strong ground motion records (0.01 - 0.2 Hz), teleseismic
 79 P waves (0.005 - 0.2 Hz) and geodetic measurements. The total moment of the model
 80 is 3.7×10^{22} N·m, equivalent to a M_w 8.98 earthquake. The model includes 396 sub-
 81 faults with 33 along-strike subfaults and 12 along-dip subfaults. Each subfaults has a
 82 $20 \times 20 \text{ km}^2$ subfault area. The model is parameterized as a planar fault with strike and
 83 dip as 195° and 14° , respectively. The model shows a single smooth, slightly elongated
 84 slip patch at the updip in zone ZC1 and towards the north of the hypocenter with peak
 85 slip away from the trench in zone N1.

86 Model R2 is from Suzuki et al. (2011), which is obtained by inverting regional ve-
 87 locity waveform integrated from accelerograms strong ground motion records (0.01 - 0.125
 88 Hz). The total moment of the model is 4.4×10^{22} N·m, equivalent to a M_w 9.03 earth-
 89 quake. The model includes 119 subfaults with 17 along-strike subfaults and seven along-
 90 dip subfaults. Each subfaults has a $30 \times 30 \text{ km}^2$ subfault area. The model is parame-
 91 terized as a planar fault with strike and dip as 195° and 13° . The model shows a sin-
 92 gle smooth, expanded, increasing slip from the hypocenter region to the trench in zone
 93 ZC1. The expanded slip reaches beyond 39°N in zone ZN1.

94 Model R3 is from Wei et al. (2012), which is obtained by inverting strong ground
 95 motion records, high-rate GPS (0 - 0.25 Hz) and geodetic measurements. The total mo-
 96 ment of the model is 5.3×10^{22} N·m, equivalent to a M_w 9.08 earthquake. The model
 97 includes 273 subfaults with 21 along-strike subfaults and 13 along-dip subfaults. Each
 98 subfault has an area of $25 \times 20 \text{ km}^2$. The model is parameterized as a planar fault with
 99 strike and dip as 201° and 10° . The model shows a major slip patch in zone ZC1, with
 100 peak slip located away from the trench. Significant shallow slip extends to the south-
 101 ern ZS1 region, reaching 36°N .

102 Model R4 is from Yue and Lay (2013), which is obtained by inverting high-rate geode-
 103 tic data and teleseismic data. The total moment of the model is 4.2×10^{22} N·m, equiv-
 104 alent to a M_w 9.02 earthquake. The model includes 120 subfaults with 15 along strike
 105 subfaults and 8 along dip subfaults. Each subfaults has a size of $30 \times 30 \text{ km}^2$. The model
 106 is parameterized as a dip-varying planar fault with the strike as 202° . The slip distri-
 107 bution is characterized by two major slip patches, with one located at the updip of the
 108 hypocenter in zone ZC1 and a similar one located at the down dip of the hypocenter in
 109 zone ZC1.

110 Model S1 is from Ide et al. (2011), which is inverted slip distribution from verti-
 111 cal broadband seismograms with a high-pass filter above 200 s using the empirical Green's
 112 function method. The total moment of the model is 4.5×10^{22} N·m, equivalent to a M_w
 113 9.04 earthquake. The model includes 231 subfaults with 21 along-strike subfaults and

114 11 along-dip subfaults. Each subfaults consist of bilinear spline basis functions with 10 km
 115 node separation. The model is parameterized as a planar fault with strike and dip as 190
 116 and 15.3. The model has a widespread slip distribution from the downdip at around 50 km
 117 depth to the trench in zone ZC1 and ZC1. The near trench slip extends from 39.5°N to
 118 36.5°S.

119 Model S2 is from Hayes (2011), which is the initial USGS model inverted from tele-
 120 seismic body waves of P, SH with a period range of 1 to 200 s and surface waves in a pe-
 121 riod range of 200 to 500 s. The total moment of the model is 4.9×10^{22} N·m, equiva-
 122 lent to a M_w 9.06 earthquake. The model includes 325 subfaults with 25 along strike sub-
 123 faults and 13 along dip subfaults. Each subfault has an area of 25×20 km². The model
 124 is parameterized as a planar fault with strike and dip as 194° and 10°. The model shows
 125 a major slip patch at the updip of the hypocenter in zone ZC1 and a secondary slip patch
 126 at the down-dip of the hypocenter in zone ZC1.

127 Model S3 is from the revised USGS finite-fault model of the Tohoku-oki earthquake,
 128 with the last update in 2018 (Goldberg et al., 2022). The model is inverted from tele-
 129 seismic body waves of P, SH with a period range of 1 to 200 s and surface waves in the
 130 period range of 200 to 500 s. The total moment of the model is 4.8×10^{22} N·m, equiv-
 131 alent to a M_w 9.05 earthquake. The model has 325 subfaults, with 25 along strike sub-
 132 faults and 13 along dip subfaults. The model is parameterized as a varying strike pla-
 133 nar fault with strike and dip as 198 and 8, 198 and 15, and 198 and 21 at the depth ranges
 134 of 3–15, 15–33, and 33–52 km. The model shows a distinctive two major slip patch with
 135 one at the north of the hypocenter and one at the south of the hypocenter. The over-
 136 all slip distribution is elongated along the strike with two minor deeper slip patches at
 137 the down-dip and north of the hypocenter in zone ZC1, reaching 50 km.

138 Model S4 is from Ammon et al. (2011), which is obtained by inverting teleseismic
 139 P waves with relative source time function inverted from Rayleigh waves and high-rate
 140 GPS recordings (lowpass 30s). The total moment of the model is 3.6×10^{22} N·m, equiv-
 141 alent to a M_w 8.98 earthquake. The model has 560 subfaults, with 50 along strike sub-
 142 faults and 14 along dip subfaults. Each subfault has a size of 15×15 km². The model
 143 is parameterized as a planar fault with strike and dip as 202° and 12°. The model shows
 144 a large smooth single-slip patch with peak slip extending from the hypocenter to the south
 145 of the hypocenter, located in the zone ZC1 and ZC1.

146 Model S5 is from Yagi and Fukahata (2011), which is obtained by inverting tele-
 147 seismic P waves in velocity with a period of 2.6 to 100 s. The total moment of the model
 148 is 5.7×10^{22} N·m, equivalent to a M_w 9.10 earthquake. The model has 250 subfaults
 149 with 25 along strike subfaults and 10 along dip subfaults. Each subfaults has a size of
 150 10×10 km². The model is parameterized as a planar fault with strike and dip as 200
 151 ° and 12°. The rake angles of all subfaults are fixed at 90 °. The model shows a major
 152 slip patch at the updip of the hypocenter, with the peak slip extending towards the trench
 153 in zone ZC1. Slip extends towards the south and deeper region in zone S2.

154 Model S6 is from Kubo and Kakehi (2013), which is obtained by inverting teleseis-
 155 mic P waves with a period of 10 to 100 s. The total moment of the model is 3.4×10^{22}
 156 N·m, equivalent to a M_w 8.95 earthquake. The model has 108 subfaults with 18 along
 157 strike subfaults and six along dip subfaults. Each subfaults has a varying size. The model
 158 is parameterized as multiple planar faults with strike and dip 185° and 7°, 197.5° and
 159 11°, and 210° and 23° along strike. The model shows a very smooth slip patch with peak
 160 slip at the updip of the hypocenter reaching the trench in zone ZC1.

161 Model T1 is from Simons et al. (2011), which is obtained by inverting tsunami and
 162 geodetic data. The total moment of the model is 7.8×10^{22} N·m, equivalent to a M_w
 163 9.19 earthquake. The model has 419 subfaults with varying subfault sizes. The model
 164 is parameterized as a curved geometry triangulated by the subfaults. The model shows

165 an elongated slip patch along the strike of the hypocenter in zones N1, ZC1 and ZC1.
 166 The elongated slip extends from 40° north to 37 °N. The model also shows a high level
 167 of heterogeneity with many smaller slip patches.

168 Model T2 is from Fujii et al. (2011), which is obtained by inverting the tsunami
 169 data. The total moment of the model is 3.8×10^{22} N·m, equivalent to a M_w 8.99 earth-
 170 quake. The model has 40 subfaults, with ten along strike subfaults and four along dip
 171 subfaults. Each subfault has a size of 50×50 km². The model is parameterized as a planar
 172 fault with strike and dip as 193° and 14°. The rake angles of all subfaults are fixed
 173 at 81°. The model shows a single and concentrated slip patch at the updip hypocenter
 174 region with slip increases towards the trench in zone ZC1.

175 Model T3 is from Saito et al. (2011), which is obtained by inverting the tsunami
 176 data. The total moment of the model is 3.8×10^{22} N·m, equivalent to a M_w 8.99 earth-
 177 quake. The model has 130 grid nodes, with 13 nodes along the strike and 10 nodes along
 178 the dip. Each node is represented by a Gaussian basis function. The model is param-
 179 eterized as a varying dip fault with a strike of 193 °. The model shows a major slip as-
 180 perity at the hypocenter region and extended slip towards the trench in zone ZC1.

181 Model T4 is from Gusman et al. (2012), which is obtained by inverting tsunami
 182 and geodetic data. The total moment of the model is 5.1×10^{22} N·m, equivalent to a
 183 M_w 9.07 earthquake. The model has 45 subfaults with nine along strike and five along
 184 dip subfaults. Each subfault has a size of 50×40 km². The model is parameterized as
 185 a varying dip fault with a strike of 202°. The model shows a smooth single slip patch
 186 at the updip of the hypocenter with significant slip at the trench in zone ZC1.

187 Model T5 is from Hooper et al. (2013), which is obtained by inverting tsunami and
 188 geodetic data. The total moment of the model is 4.0×10^{22} N·m, equivalent to a M_w
 189 9.00 earthquake. The model has 234 subfaults with 18 along strike subfaults and 13 along
 190 dip subfaults. Each subfault has a size of 25×20 km². The model is parameterized as
 191 a dip varying fault with a strike of 194°. The model has a major slip patch at the up-
 192 dip of the hypocenter in zone ZC1. Narrow and elongated slip features from 20 km to
 193 40 km extend near the hypocenter and towards the south of the hypocenter. A north-
 194 ern minor slip patch at the depth of 12 km in zone ZN1 also appears in the slip distri-
 195 bution.

196 Model T6 is from Satake et al. (2013), which is obtained by inverting tsunami and
 197 geodetic data. The total moment of the model is 4.2×10^{22} N·m, equivalent to a M_w
 198 9.02 earthquake. The model has 55 subfaults, with 11 along strike subfaults and five along
 199 dip sub faults. Each subfault has a size of 50×50 km². The model is parameterized as
 200 a dip-varying planar fault with a strike of 193°. The model shows a smooth large expand-
 201 ing slip patch in the updip of the hypocenter with increasing slip toward the trench in
 202 zone ZC1.

203 Model T7 is from Romano et al. (2014), which is obtained by inverting tsunami
 204 and geodetic data. The total moment of the model is 5.7×10^{22} N·m, equivalent to a
 205 M_w 9.10 earthquake. The model has 398 subfaults. The model is parameterized as a curved
 206 fault with the subfaults subdivided into patches of variable size: 24 km \times 14 km, 24 km \times 24
 207 km, 35 \times 35 km² at depth ranges of 2-15, 15-40, 40-60 km. The model shows a similar
 208 overall slip structure as model G6 with a large expanding slip patch in the updip of the
 209 hypocenter with increasing slip toward the trench in zone ZC1. The model shows a high
 210 level of slip heterogeneity with many small slip patches.

211 Model T8 is from Kubota et al. (2022), which is obtained by inverting Tsunami
 212 and geodetic data. The total moment of the model is 5.1×10^{22} N·m, equivalent to a
 213 M_w 9.07 earthquake. The model has 434 subfaults triangulating the 3D fault surface,
 214 with the length of each side of the triangle about 10 km. The model shows a smooth large

215 slip patch at the updip of the hypocenter with increasing slip towards the trench in zone
 216 ZC1. The model shows near trench slip at the northern section in zone ZN1 reaching 39.5°N.

217 Model J1 is from Yokota et al. (2011), which is jointly inverted from geodetic, strong
 218 ground motion (0.01 - 0.1 Hz), teleseismic P wave (0.002 - 0.25 Hz) and tsunami obser-
 219 vations. The total moment of the model is 4.2×10^{22} N·m, equivalent to a M_w 9.02 earth-
 220 quake. The model has 96 subfaults, with 16 along strike subfaults and five along dip sub-
 221 faults. Each subfault has a size of 30×30 km². A varying dip fault geometry is used
 222 with a strike angle of 200°. The model shows a concentrated slip at the hypocenter along
 223 the 20 km depth in zones ZC1 and ZC1. The slip extends to the north, reaching 39.5°N.

224 Model J2 is from Minson et al. (2014), which is jointly inverted from the tsunami
 225 and high-rate GPS data (0.005 - 0.1 Hz). The total moment of the model is 5.3×10^{22}
 226 N·m, equivalent to a M_w 9.08 earthquake. The model has 219 subfaults, with 24 along
 227 strike subfaults and nine along dip subfaults. Each subfault has a size of around $30 \times$
 228 30 km². The model is parameterized as a varying dip fault with a strike of 194°. The
 229 model shows a major slip patch at the hypocenter in zones ZC1 and ZC1. Extensive near
 230 trench slip was also imaged by the model extending from 39°N to 37°N. The model also
 231 shows a higher level of slip heterogeneity with patches of slip across the major slip area
 232 and other parts of the fault.

233 Model J3 is from Bletery et al. (2014), which is obtained by inverting the geode-
 234 tic, high-rate geodetic (0.01 - 0.08 Hz), strong ground motion (double-integrated to dis-
 235 placement and filtered between 0.01 and 0.08 Hz), teleseismic P (1.25-100 s) and SH waves
 236 (2.5-100 s) and tsunami data. The total moment of the model is 3.5×10^{22} N·m, equiv-
 237 alent to a M_w 8.96 earthquake. The model has 187 subfaults with varying subfault sizes.
 238 The model is parameterized as a curved fault. The model shows a patchy shallow slip
 239 distribution with most slip confined at the updip of the hypocenter region in zone ZC1.
 240 The near trench slip extends from 37°N to 39.3°N.

241 Model J4 is from Melgar and Bock (2015), which is obtained by inverting the col-
 242 located seismogendetic recordings and tsunami data. The total moment of the model is
 243 5.5×10^{22} N·m, equivalent to a M_w 9.09 earthquake. The model has 189 subfaults, with
 244 21 along strike subfaults and nine along dip subfaults. Each subfault has a size of $25 \times$
 245 25 km². The model is parameterized as a curved fault. The model shows a major slip
 246 patch at the updip of the hypocenter with a confined large slip at the shallowest 10 km
 247 section of the fault in zone ZC1. Small near trench slip patches also appear in 40°N and
 248 36°N.

249 J4 model uses 20 colocated seismo-geodetic stations to invert the slip distribution.
 250 The displacement and velocity data are filtered between 0 and 0.5 Hz to match their greens
 251 function. However, they discovered that the coherence greatly depleted for wave period
 252 shorter than 7-8 seconds.

253 Model J5 is from Yamazaki et al. (2018), which is iteratively inverted from the geode-
 254 tic, teleseismic and tsunami data. The total moment of the model is 4.0×10^{22} N·m,
 255 equivalent to a M_w 9.00 earthquake. The model has 240 subfaults with 20 along strike
 256 subfaults and 12 along dip subfaults. Each subfault has a size of 20×20 km². The model
 257 is parameterized as a varying dip fault. The model shows a major L shape slip patch at
 258 the updip of the hypocenter with a confined large slip at the shallowest 10 km section
 259 of the fault and extended slip to 20 km dip at the south of the hypocenter in zone ZC1.
 260 Secondary features of the slip include a near trench slip at 39.5 °N in zone ZN1 and slip
 261 reaching 40 km depth at 37 °N in zone S2.

Text S2: Teleseismic Displacement Waveforms Sensitivity Analysis

We compute teleseismic synthetic waveforms using the single-time window method with an assumed slip-rate function. We systematically compare synthetics from different slip-rate functions with varying duration. We use cosine, triangular, and regularized Yoffe functions to compute the synthetics (Figure S16). We pair the slip-rate functions with the same peak-slip-rate-time distribution from model S3 model for a consistent comparison. The comparison with the observations is summarized in Table S2.

We find that the teleseismic synthetics are insensitive to the shape and duration of the slip-rate functions. The synthetics are highly similar to the observations, with a median ≥ 0.82 correlation coefficient for all slip-rate functions. Figure S20 compares the synthetics with Yoffe, cosine and triangle functions, all having the same rise-time of 16 s and duration of around 32 s. The synthetics show negligible differences, suggesting that teleseismic waveforms are insensitive to the shape of the slip-rate function, given similar rise-time and duration.

We further compare the teleseismic data sensitivity to the decay rate and duration of the slip-rate function. We apply the Yoffe function with the same-rise time but with extended durations (40, 28, and 55 s), as shown in Figure S16. The synthetics show highly similar shapes with varying amplitudes (Figure S21). Particularly, the synthetics of the Yoffe function with varying duration show the same peak and trough timing in the synthetic waveforms. Hence, teleseismic waveforms seem to have limited sensitivity to the variation of the Yoffe function, confirming that our method with regularized Yoffe function for all models can effectively describe the slip-rate function for computing the teleseismic synthetics.

We further examine the rupture propagation effects on the teleseismic waveforms. We compare and validate different models' peak-slip-rate-time (PSRT) distributions, which describe the rupture front evolution of the respective models. We use three different slip models: Models S3, S6, and J5, all of which use teleseismic waveforms to invert slip distributions. Model S3 uses the single-time window method to describe the slip-rate evolution, while models S6 and J5 use the multi-time window method. We extract the PSRT of each projected model and map it to the model S3 slip distribution at the 16 km scale. We use the uniform regularized Yoffe function for each subfault and align it with the peak-slip-rate time accordingly.

The three PSRT distributions agree on major slip episodes but show varying complexity (Figure S23). Models S3 and J3 show a relatively smooth and regular expansion in the first 50 s, followed by a complex and irregular pattern for the rest of the rupture, associated with the major slip patch in ZC1. In contrast, model S6 shows a consistently smooth PSRT evolution. This smooth evolution continues through the major rupture area but with an increasing rupture speed. All three models show similar peak-slip-rate timing in the major slip patch. They suggest that the peak-slip-rate time for the major slip patch ranges from 40–80 s.

Synthetics using the S6 and J3 PSRT distributions show satisfactory fitting with the observed seismograms (Figure S24), with both synthetics reaching a correlation coefficient of 0.75. Comparatively, we compute the synthetics of models S6 and S3 using a uniform Yoffe function aligned with their peak-slip-rate time, respectively. The resulting synthetics have correlation coefficients with the observations of 0.71 for model S6 and 0.73 for model J3. The slight decrease in correlation results from our simplification of the complex slip-rate function from the multi-time-window method. Nevertheless, our comparison validates that the teleseismic waveforms are sensitive to the rupture propagation effects, and the peak-slip-rate time distribution of model S3 is effective in describing the slip-rate evolution.

312 **Text S3: Teleseismic Velocity Sensitivity Analysis**

313 Our teleseismic data validation test in Section 4.2 shows that teleseismic displacement
 314 data are insensitive to the small-scale slip features. The displacement synthetics
 315 of the body waves have a dominant period of 20–30 s, which corresponds to a 90–120 km
 316 wavelength (Figure 11). We further test the sensitivity of teleseismic velocity waveforms,
 317 which contain more higher-frequency signals than the displacement waveforms, with a
 318 dominant period of around 15 s for the body waves. We follow the same procedure in
 319 Section 4.2.

320 We find that the teleseismic velocity waveforms have additional sensitivity to the
 321 fault geometry as compared to the displacement waveforms (Figure S26). We investi-
 322 gate the slip-rate function effects on the teleseismic velocity waveforms following the same
 323 procedure in Section 4.2.2. Our tests show that the velocity records have limited sen-
 324 sitivity to the slip-rate function (Figures S29 and S30). We explore the rupture prop-
 325 agation effects on the teleseismic velocity waveforms. We compare the slip-rate onset time
 326 alignment with the original S3 model onset time, peak-slip-rate time, and constant rup-
 327 ture velocity. We find that rupture propagation has a strong impact on the teleseismic
 328 velocity synthetics. Figure S29 shows synthetics using the original onset time alignment
 329 and a uniform Yoffe slip-rate function, resulting in a correlation of 0.52, while the orig-
 330 inal projected model has a correlation of 0.76. The synthetics using the PSRT alignment
 331 and a uniform Yoffe slip-rate function fit the observed waveforms, with a correlation of
 332 0.71 (Figure S28). Similar to the displacement waveforms, both the constant rupture speed
 333 and two-step rupture speed failed to produce reasonable waveform fits (Figure S28).

334 We also apply the PSRT approach using the PSRT distributions from models S6
 335 and J3. Following the same procedure in Section 4.2.3, we compute the teleseismic ve-
 336 locity synthetics using the S3 slip distribution and the PRST distributions from mod-
 337 els S6 and J3. Both sets of synthetics can fit the long-period waveforms but not the short-
 338 period signals (Figure S32). We compute synthetics using the PSRT from model S3 and
 339 the slip distributions from models S6 and J3. The synthetics are similar to those from
 340 the S3 slip distribution.

341 We follow the same procedure and compute teleseismic synthetics velocity wave-
 342 forms using the final slip distributions at the 16, 32, and 64 km scales for all models. Fig-
 343 ure S33 shows teleseismic body-wave velocity synthetics for all models at a 16 km scale.
 344 The synthetics fit the first-order features of the teleseismic velocity observations. For ex-
 345 ample, the synthetics show accurate peaks and troughs for SH and SV waves at station
 346 BRVK. However, synthetics variations are more significant in the teleseismic velocity wave-
 347 forms than the displacement waveforms. Synthetics SH waves from different slip mod-
 348 els show contrasting waveform shapes around 50–150 s from S wave arrivals at both sta-
 349 tions COR and HNR. The variations in velocity waveforms suggest a possible higher sen-
 350 sitivity for secondary slip features. We compute the correlation coefficients of the syn-
 351 thetic body waves with the observations. The velocity seismic synthetics of all models
 352 at three scales show a lower correlation ranges from 0.5 to 0.7, with the SH synthetics
 353 slightly better than P and SV synthetics. However, it is worth noting that the correla-
 354 tion value of the velocity waveforms is also compatible with typical inversion results (e.g.
 355 Melgar & Bock, 2015).

Text S4: High-rate GNSS and Strong-Ground Motion Sensitivity Analysis

We compute the High-rate GNSS and strong ground motion synthetics following the same procedure of Section 4.2 Teleseismic Data analysis. The synthetics are computed using the open-source software Instaseis (van Driel et al., 2015). This method uses pre-computed Green’s function databases, calculated using the anisotropic version of the Preliminary Reference Earth Model (PREM) and the AxiSEM method up to 2 s period band (Dziewonski & Anderson, 1981; Nissen-Meyer et al., 2014). Green’s function is convoluted with the source time function either with the original finite-fault models or the unified source-time function, with the same Yoffee-slip rate function aligned with the S3 peak-slip-rate time.

The synthetics are compared with the strong-ground motion records and the horizontal high-rate GNSS record. The strong ground motion records are doubled-integrated into displacement and band-passed between 10-100s, while the high-rate GNSS records are lowpass-filtered at 10 seconds. The frequency range is compatible with the regional seismic and joint-inversion models’ data processing procedure.

To validate the geometric effects of the projection, we compare the synthetics from the original J4 finite-fault model and the projected J4 finite-fault model. We use the original multi-time-window method to compute the synthetics. Figure S35 compares the differences between the two models. Both sets of synthetics demonstrate high similar waveforms, suggesting the projected fault geometry can reproduce the observed regional seismic records.

Similarly, we compare the original and projected J4 finite-fault models synthetics with the high-rate GNSS records (Figure S38). Both synthetics show overlapping waveforms with the observations. In addition, we compare the synthetics with the static offset computed by 3D Green’s function in Section 4.1, as shown by the dashed grey lines in Figure S38. All synthetics including the original J4 model, and projected J4 model show consistency with the observations and the deformation by 3D velocity structure Green’s function.

Table S1. Offshore geodetic stations

Station	Longitude	Latitude	Depth [km]	Eastward displacement [m]	Northward displacement [m]	Vertical displacement [m]
GJT3	143.483	38.273	3.281	29.500	-11.000	3.734
GJT4	142.833	38.407	1.445	14.000	-5.000	3.500
MYGI	142.917	38.084	1.700	22.100	-10.400	3.100
MYGW	142.433	38.153	1.100	14.300	-5.100	-0.800
FUKU	142.083	37.166	1.200	4.400	-1.700	0.900
KAMS	143.263	38.636	2.200	21.100	-8.900	1.500
KAMN	143.363	38.887	2.300	13.800	-5.800	1.600
CHOS	141.670	35.500	1.600	0.950	-0.950	0.400
TJT1	143.796	38.209	5.758	N.A.	N.A.	5.093
P02	142.502	38.500	1.100	N.A.	N.A.	-0.801
P06	142.584	38.634	1.250	N.A.	N.A.	-0.975
TM1	142.780	39.236	1.500	N.A.	N.A.	-0.800
TM2	142.446	39.256	1.000	N.A.	N.A.	-0.300

Table S2. Summary of teleseismic P wave displacement synthetics performance on changing geometry, subfault size, slip-rate, and rupture front time-alignment.

Slip model	subfault ^a	slip-rate ^b	slip-rate alignment ^c	P wave correlation ^d	P wave variance reduction ^d	Figure ^e
S3	original	original	original	0.90 (0.01)	80% (5%)	FigS17
S3 projected	original	original	original	0.89 (0.01)	68% (28%)	FigS17
S3 projected	original	Yoffe16(40)	original	0.84 (0.01)	65% (15%)	FigS18
S3 projected	original	Yoffe16(40)	S3 PSRT	0.88 (0.01)	74% (9%)	FigS18
S3 projected	original	original	Vr 2.0 km/s	0.65 (0.01)	27% (30%)	FigS19
S3 projected	original	original	Vr 1.5 & 2.0 km/s	0.65 (0.01)	31% (12%)	FigS19
S3 projected	original	Cosine16	S3 PSRT	0.88 (0.01)	71% (18%)	FigS20
S3 projected	original	Tri 16	S3 PSRT	0.88 (0.01)	74% (11%)	FigS20
S3 projected	original	Yoffe16(48)	S3 PSRT	0.85 (0.01)	71% (5%)	FigS21
S3 projected	original	Yoffe16(55)	S3 PSRT	0.82 (0.01)	66% (2)	FigS21
S3 projected	16 km	Yoffe16(40)	S3 PSRT	0.82 (0.01)	63% (17%)	FigS22
S6 projected	16 km	Yoffe16(40)	S3 PSRT	0.77 (0.03)	47% (36%)	FigS22
J3 projected	16 km	Yoffe16(40)	S3 PRST	0.76 (0.02)	48% (17%)	FigS22
G4 projected	16 km	Yoffe16(40)	S3 PSRT	0.76 (0.04)	50% (24%)	FigS25
R3 projected	16 km	Yoffe16(40)	S3 PRST	0.75 (0.04)	48% (73%)	FigS25
S3 projected	16 km	Yoffe16(40)	S6 PSRT	0.75 (0.03)	49% (41%)	FigS24
S3 projected	16 km	Yoffe16(40)	J3 PSRT	0.75 (0.02)	54% (18%)	FigS24

^a subfault size of the finite fault model, original S3 model subfault size is 25 km × 16.6 km

^b Yoffe16(): Yoffe function with rise time 16s with duration in parentheses; Cosine16: Cosine function with rise time 16; Tri16: Triangle function with rise time 16. The slip-rate functions are shown in Figure S16

^c Vr km/s - Rupture onset by constant rupture speed; Rupture onset - follow model rupture onset time; PSRT - peak slip rate time (Figure S15 and Figure S23).

^d median (standard deviation)

^e supplementary figure showing the synthetics and observed waveforms comparison

Table S3. Summary of teleseismic P wave velocity synthetics performance on changing geometry, subfault size, slip-rate, and rupture front time-alignment.

Slip model	subfault ^a	slip-rate ^b	slip-rate alignment ^c	P wave correlation ^d	P wave variance reduction ^d	Figure ^e
S3	original	original	original	0.81 (0.01)	55% (25%)	FigS26
S3 projected	original	original	original	0.76 (0.01)	44% (65)	FigS26
S3 projected	original	Yoffe16(40)	original	0.52 (0.02)	20% (1%)	FigS27
S3 projected	original	Yoffe16(40)	S3 PSRT	0.71 (0.02)	50% (8%)	FigS27
S3 projected	original	original	Vr 2.0 km/s	0.48 (0.01)	21% (2%)	FigS28
S3 projected	original	original	Vr 1.5 & 2.0 km/s	0.54 (0.01)	22% (24%)	FigS28
S3 projected	original	Cosine16	S3 PSRT	0.74 (0.02)	52% (21%)	FigS29
S3 projected	original	Tri 16	S3 PSRT	0.72 (0.02)	50% (8%)	FigS29
S3 projected	original	Yoffe16(48)	S3 PSRT	0.68 (0.02)	45% (4%)	FigS30
S3 projected	original	Yoffe16(55)	S3 PSRT	0.67 (0.02)	42% (3)	FigS30
S3 projected	16 km	Yoffe16(40)	S3 PSRT	0.62 (0.01)	32% (11%)	FigS31
S6 projected	16 km	Yoffe16(40)	S3 PSRT	0.53 (0.02)	15% (19%)	FigS31
J3 projected	16 km	Yoffe16(40)	S3 PSRT	0.56 (0.03)	23% (16%)	FigS31
S3 projected	16 km	Yoffe16(40)	S6 PSRT	0.58 (0.02)	32% (13%)	FigS32
S3 projected	16 km	Yoffe16(40)	J3 PSRT	0.55 (0.02)	28% (13%)	FigS32

^a subfault size of the finite fault model, original S3 model subfault size is 25 km × 16.6 km

^b Yoffe16(): Yoffe function with rise time 16s with duration in parentheses; Cosine16: Cosine function with rise time 16; Tri 6: Triangle function with rise time 16. The slip-rate functions are shown in Figure S16

^c Vr km/s - Rupture onset by constant rupture speed; Rupture onset - follow model rupture onset time; PSRT - peak slip rate time (Figure S15 and Figure S23).

^d median (standard deviation)

^e supplementary figure showing the synthetics and observed waveforms comparison

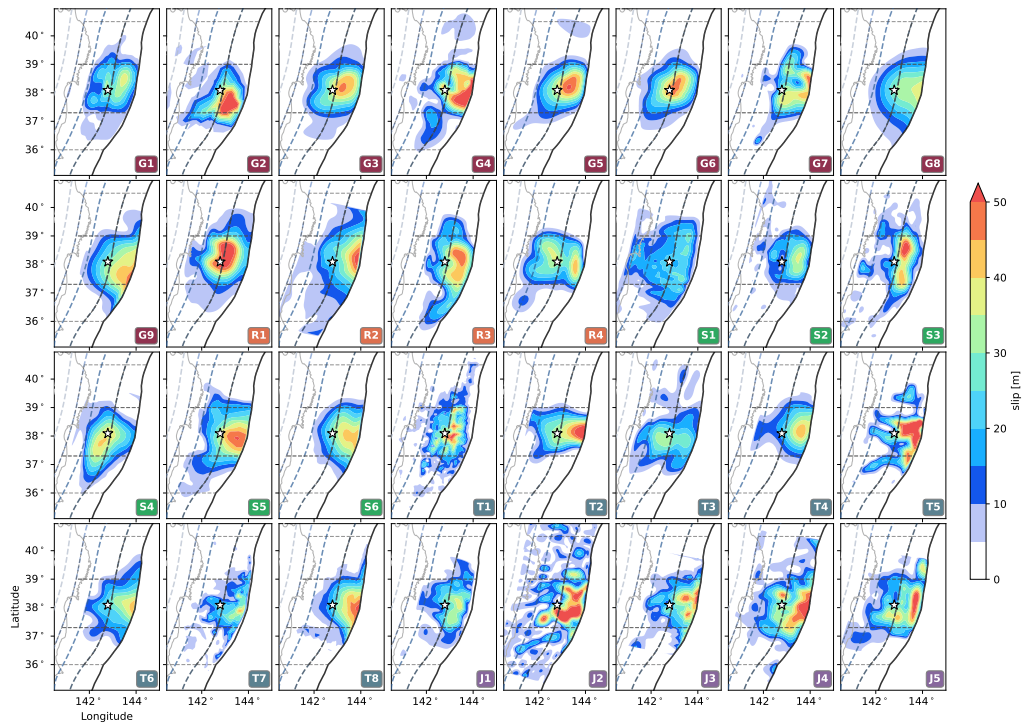


Figure S1. Slip distribution of the 32 re-parameterized finite fault models with 1 km subfault size. Slip distribution are shown as color contours. All model acronyms are defined in Figure 1 and detailed in Text S1. Grey lines indicate the six zones listed in Figure 4.

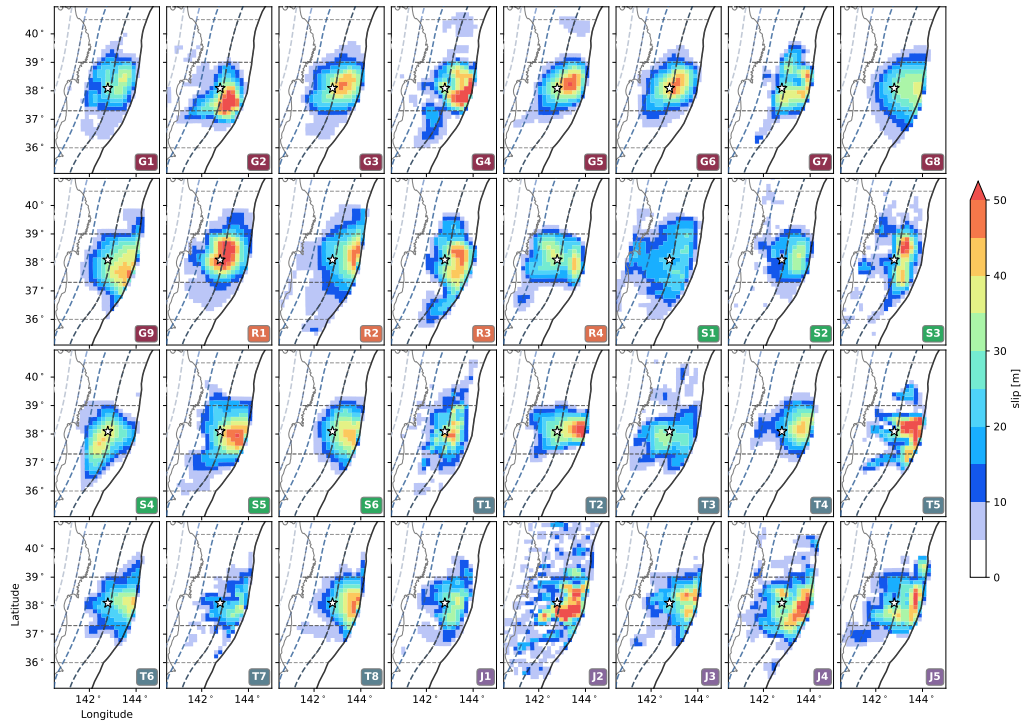


Figure S2. Slip distribution of the 32 re-parameterized finite fault models with 16 km sub-fault size. Same plotting style as Figure S1. Slip distributions are shown as color contours. All model acronyms are defined in Figure 1 and detailed in Text S1.

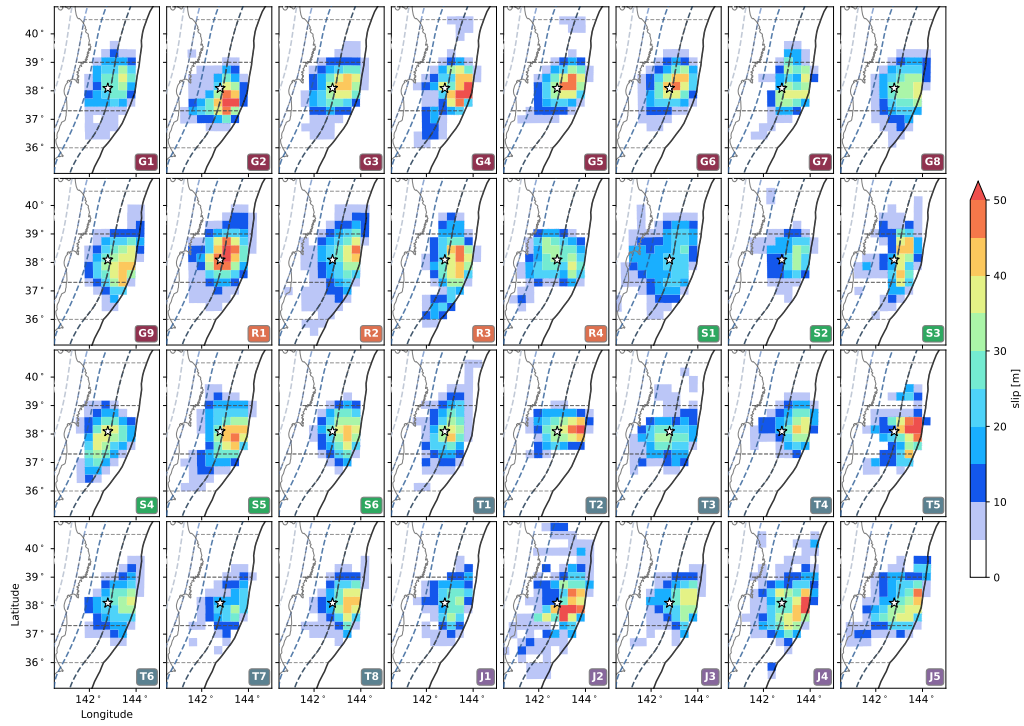


Figure S3. Slip distribution of the 32 re-parameterized finite fault models with 32 km sub-fault size. Same plotting style as Figure S1. Slip distributions are shown as color contours. All model acronyms are defined in Figure 1 and detailed in Text S1.

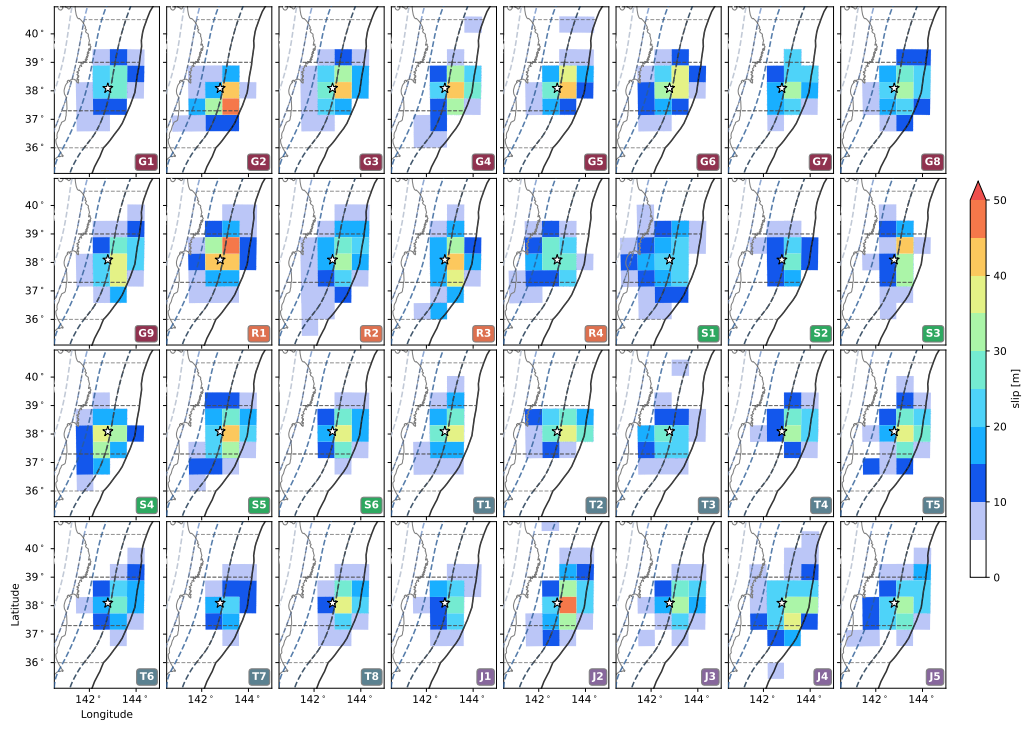


Figure S4. Slip distribution of the 32 re-parameterized finite fault models with 64 km sub-fault size. Same plotting style as Figure S1. Slip distributions are shown as color contours. All model acronyms are defined in Figure 1 and detailed in Text S1.

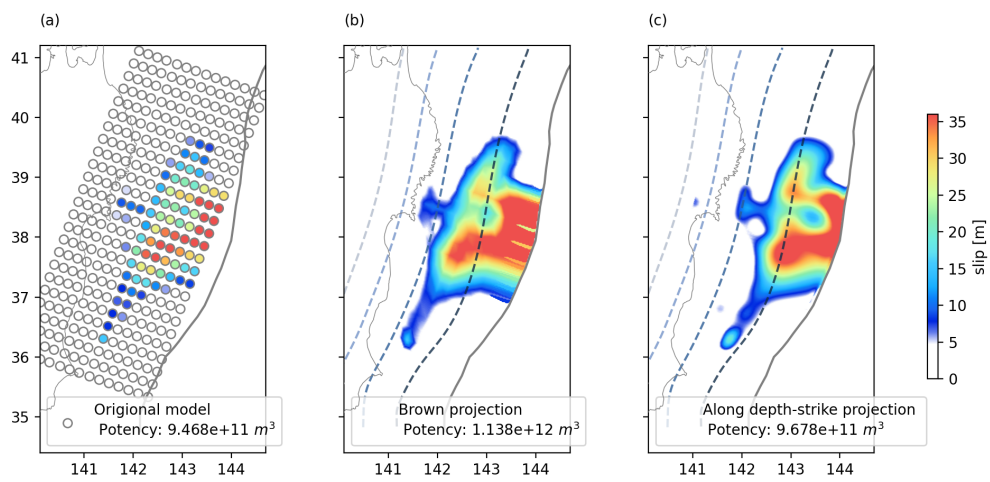


Figure S5. Comparison of (a) the original G7 model (Zhou et al., 2014), (b) the projected model using the Brown method, and (c) the projection method of this study. Inset indicates the total potency, defined as the slip times the subfault area. Solid line delineates the trench location. Dashed lines indicate the Slab 2.0 model with a 20 km depth interval.

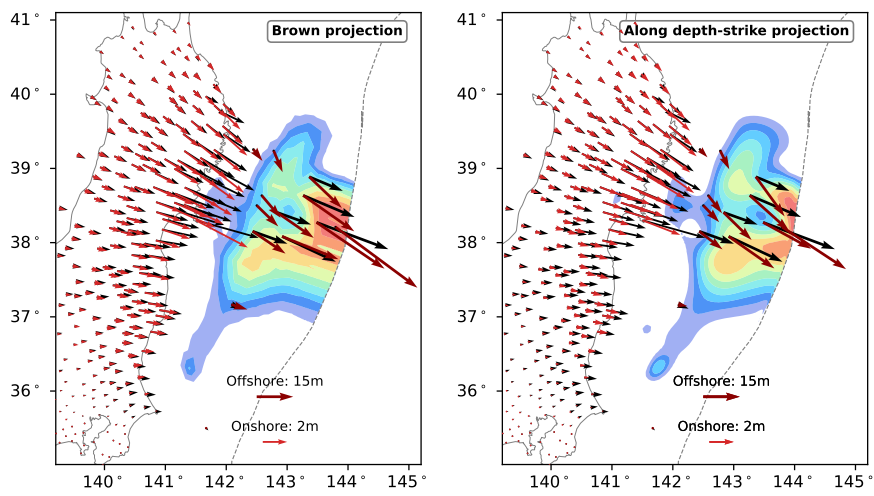


Figure S6. Comparison of the onshore and offshore horizontal displacements by (a) the projected model using the Brown method, and (b) the projection method of this study. Black and red arrows are the observations and synthetics respectively. Dotted line indicates the trench line. Color-filled contour shows the projected slip distribution.

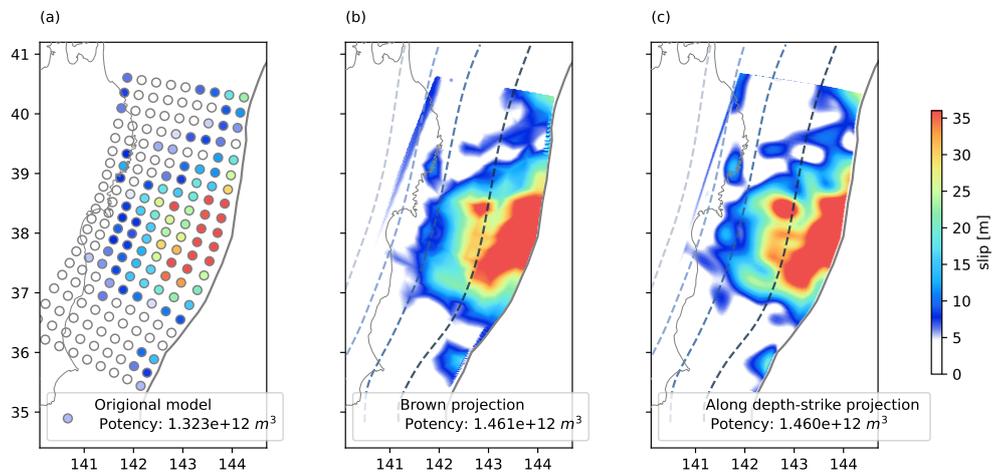


Figure S7. Comparison of (a) the original J4 model (Melgar & Bock, 2015), (b) the projected model using the Brown method, and (c) the projection method of the study. Inset indicates the total potency, defined as the slip times the subfault area. Solid line delineates the trench location. Dashed lines indicate the Slab 2.0 model with a 20 km depth interval. The J4 model was obtained using the Slab 1.0 geometry.

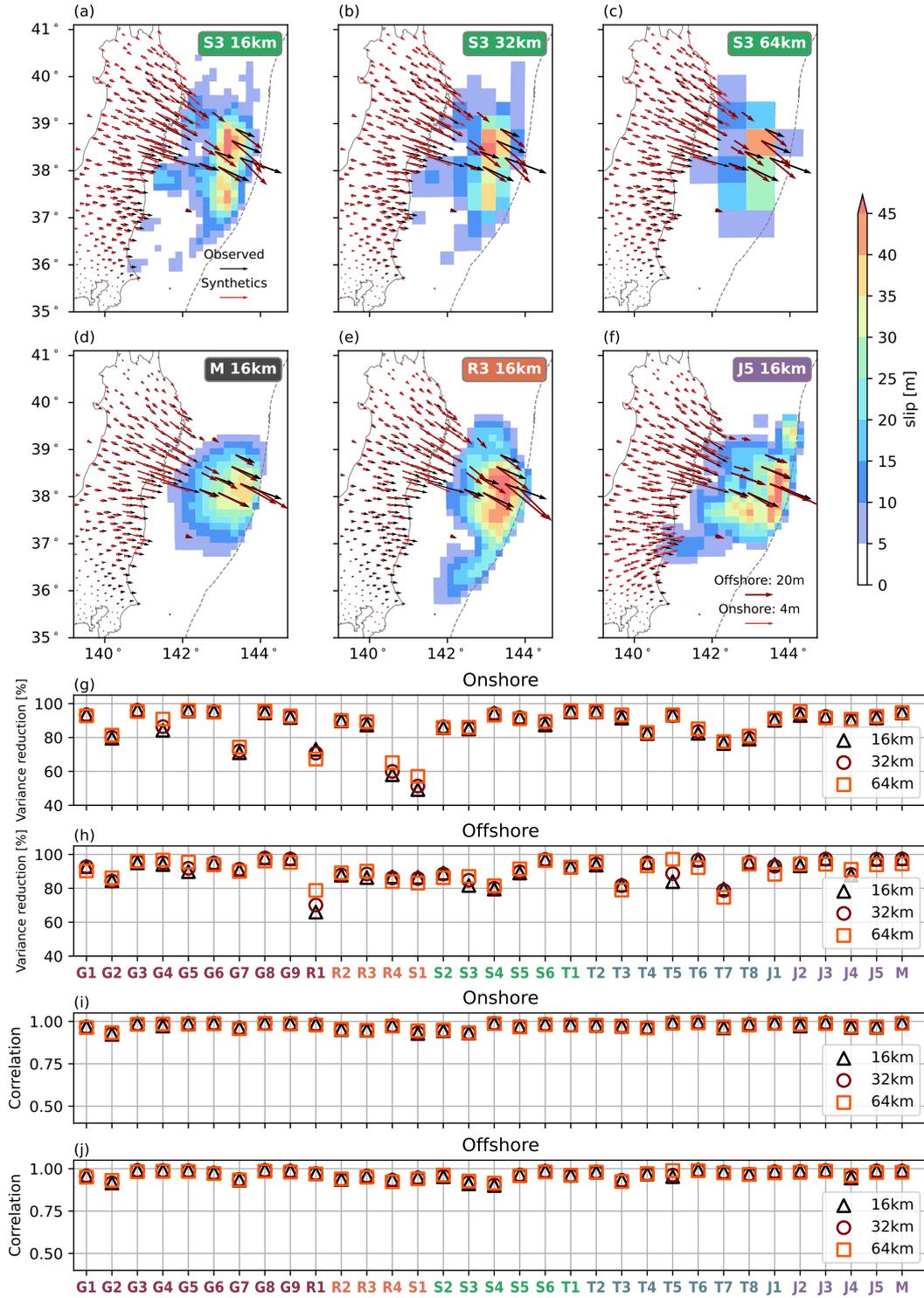


Figure S8. Onshore and offshore horizontal geodetic displacement observations (red arrows) and synthetics (black arrows), and their correlation and variance reduction values. (a)–(c) synthetic (black) and observed (red) horizontal geodetic displacements of model S3 at the 16 (a), 32 (b), and 64 km (c) scales. (d)–(f) geodetic synthetics and observations of model M (d), R3 (e), J5 (f) at the 16 km scale. (g) variance reduction values between the onshore geodetic synthetics and observations at the 16, 32, and 64 km scales. (h) variance reduction values between the offshore geodetic synthetics and observations at the 16, 32, and 64 km scales. (i) Correlation coefficients between the onshore geodetic synthetics and observations at the 16, 32, and 64 km scales. (j) Correlation coefficients between the offshore geodetic synthetics and observations at the 16, 32, and 64 km scales.

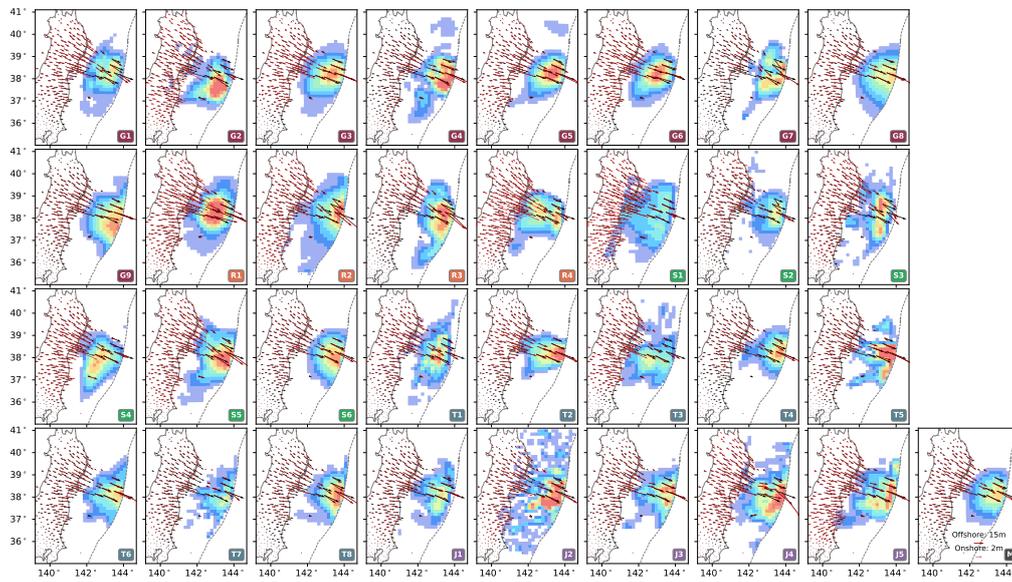


Figure S9. Onshore and offshore horizontal geodetic displacement observations (red arrows) and synthetics (black arrows) of all 33 models in 16 km scale.

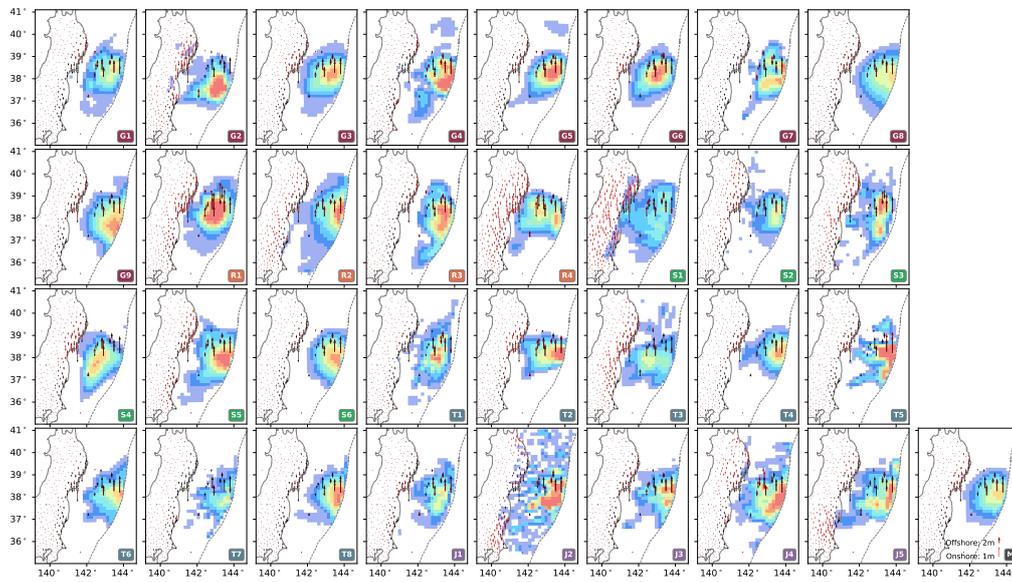


Figure S10. Onshore and offshore vertical geodetic displacement observations (red arrows) and synthetics (black arrows) of all 33 models in 16 km scale.

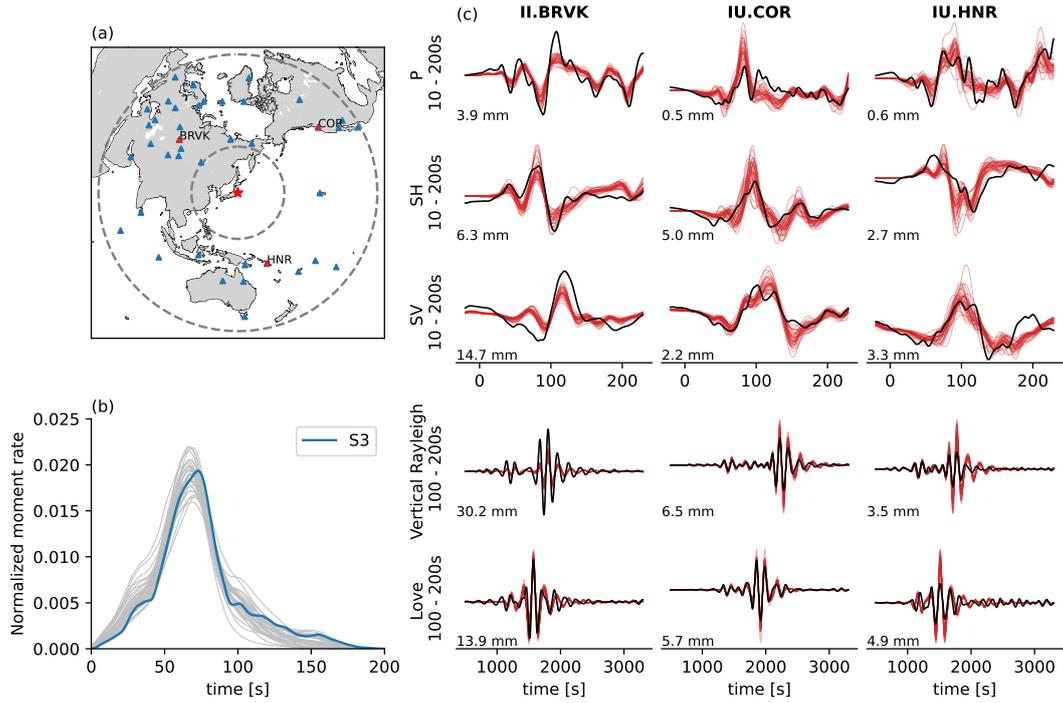


Figure S11. Comparison of teleseismic observations and synthetics at 32 km scale. (a) Map view of 40 II and IU stations used in the analysis. Red triangles are the stations in (c). Dotted circles show epicentral distances of 30^{circ} and 90^{circ} , respectively. (b) Normalized moment rate functions of the original S3 model and the other 32 finite-fault models and the median model. (c) Synthetic and observed teleseismic waveforms. Black lines are the observed waveforms; red lines are the synthetic waveforms from the 32 finite-fault models and the median model. Five rows are P wave, SH wave, SV wave, Rayleigh wave, and Love wave, respectively. Amplitudes of the observed waveforms are labeled at the lower-left corner of each waveform plot.

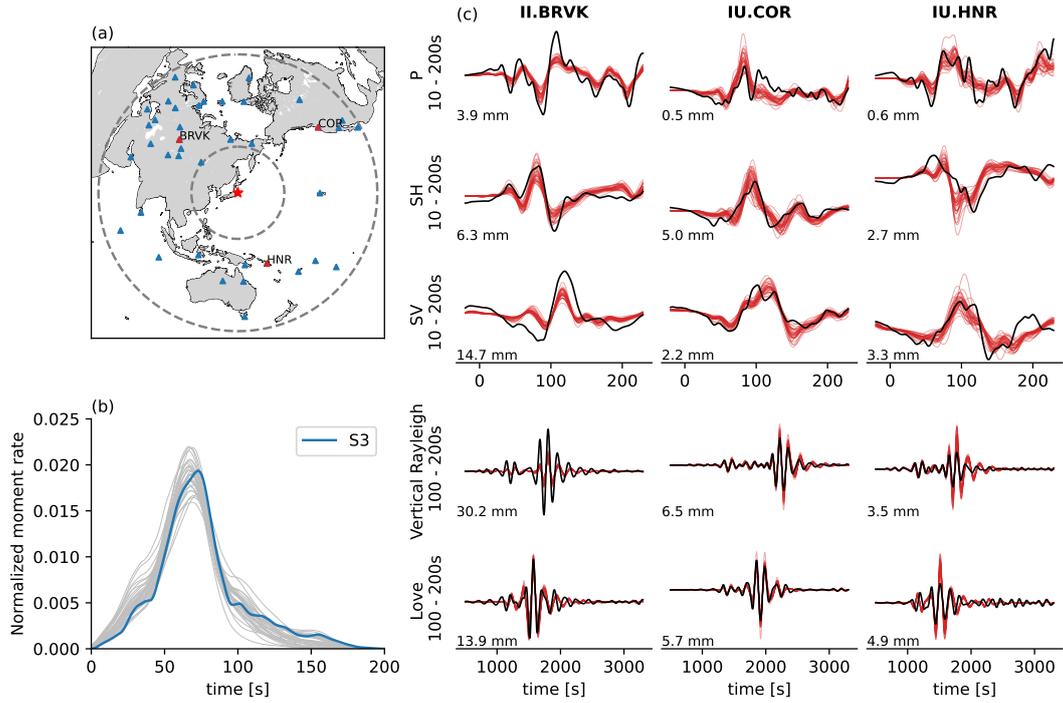


Figure S12. Comparison of teleseismic observations and synthetics at a 64 km scale. (a) Map view of 40 II and IU stations used in the analysis. Red triangles are the stations in (c). Dotted circles show epicentral distances of 30^{circ} and 90^{circ} , respectively. (b) Normalized moment rate functions of the original S3 model and the other 32 finite-fault models and the median model. (c) Synthetic and observed teleseismic waveforms. Black lines are the observed waveforms; red lines are the synthetic waveforms from the 32 finite-fault models and the median model. Five rows are P wave, SH wave, SV wave, Rayleigh wave, and Love wave, respectively. Amplitudes of the observed waveforms are labeled at the lower-left corner of each waveform plot.

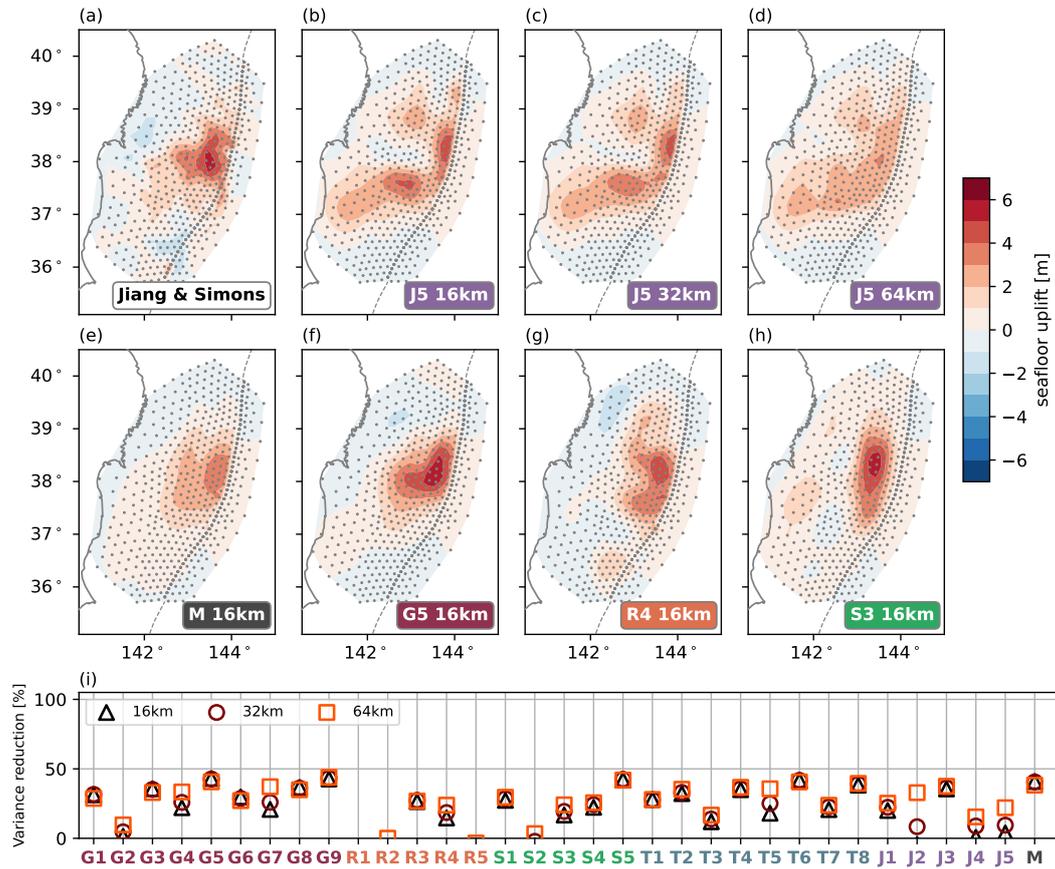


Figure S13. Seafloor uplift model of Jiang and Simons (2016) (model SJS), seafloor uplift synthetics from the finite-fault models, and their variance reduction values between the synthetics with model SJS. Grey dots show the modeled grid points. (a) Model SJS. (b)–(d) Synthetic seafloor uplift of model J5 model at the 16 (b), 32 (c), and 64 km (d) scales, respectively. (e)–(h) Synthetic seafloor uplift of the median slip model, models G5, R4, and S3 at a 16 km scale. (i) variance reduction values between model SJS and synthetics of the 32 finite-fault models and the median model at the 16, 32, and 64 km scales.

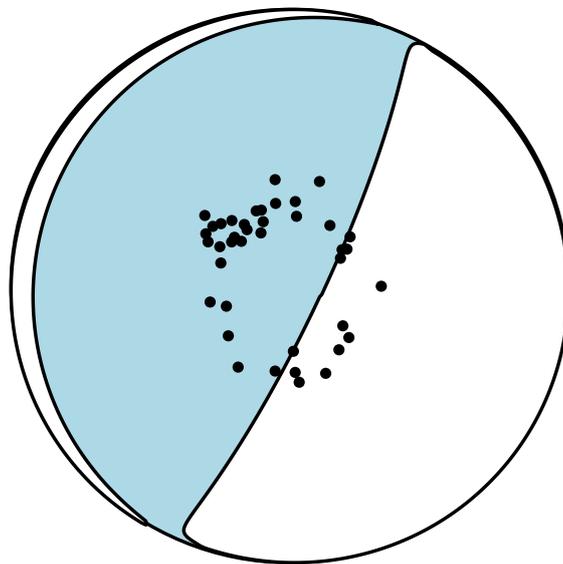


Figure S14. Azimuth and takeoff angle of the teleseismic stations used in the analysis with the Tohoku-Oki earthquake moment tensor from GCMT.

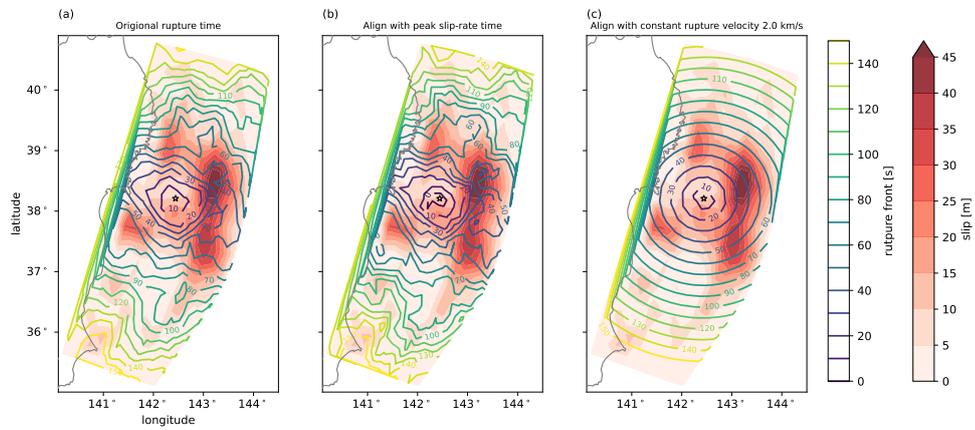


Figure S15. Rupture onset time alignment for the teleseismic synthetics. Panel a shows the original rupture onset time of the S3 model. Panel b shows the alignment with the peak-slip-rate time (PSRT) of the S3 model. Panel c shows the alignment with the constant 2.0 m/s rupture velocity.

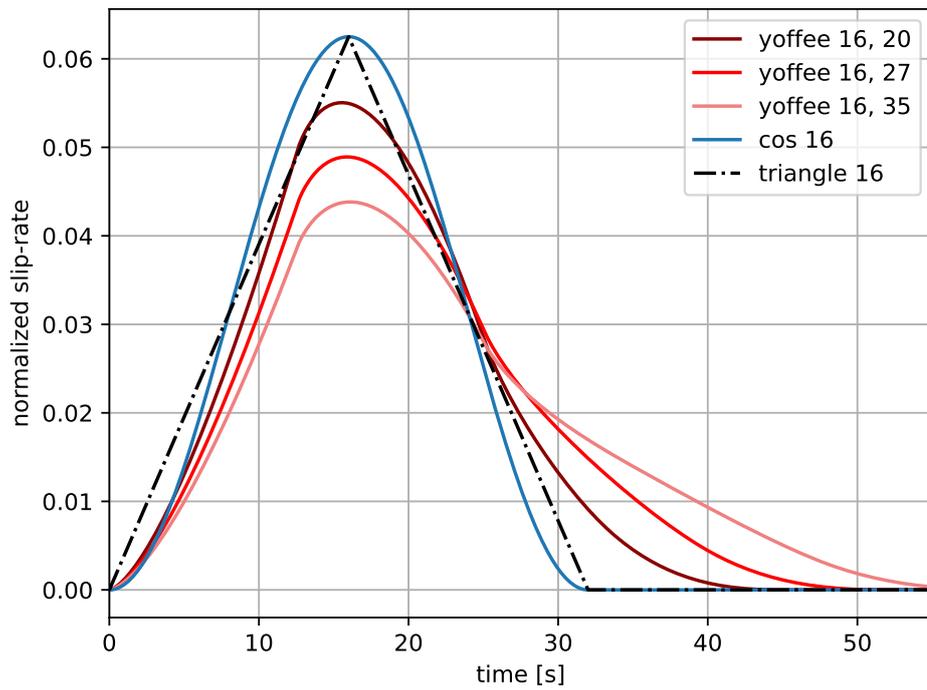


Figure S16. Normalized slip-rate functions evaluated in the teleseismic synthetics. Slip-rate functions include three sets of Yoffe slip-rate functions (reds) with the same rise-time of 16 s and varying duration of 40, 48, and 55 s, and a cosine function with a 16 s rise time (blue) and a symmetrical-triangular function with a rise time of 16 s (grey).

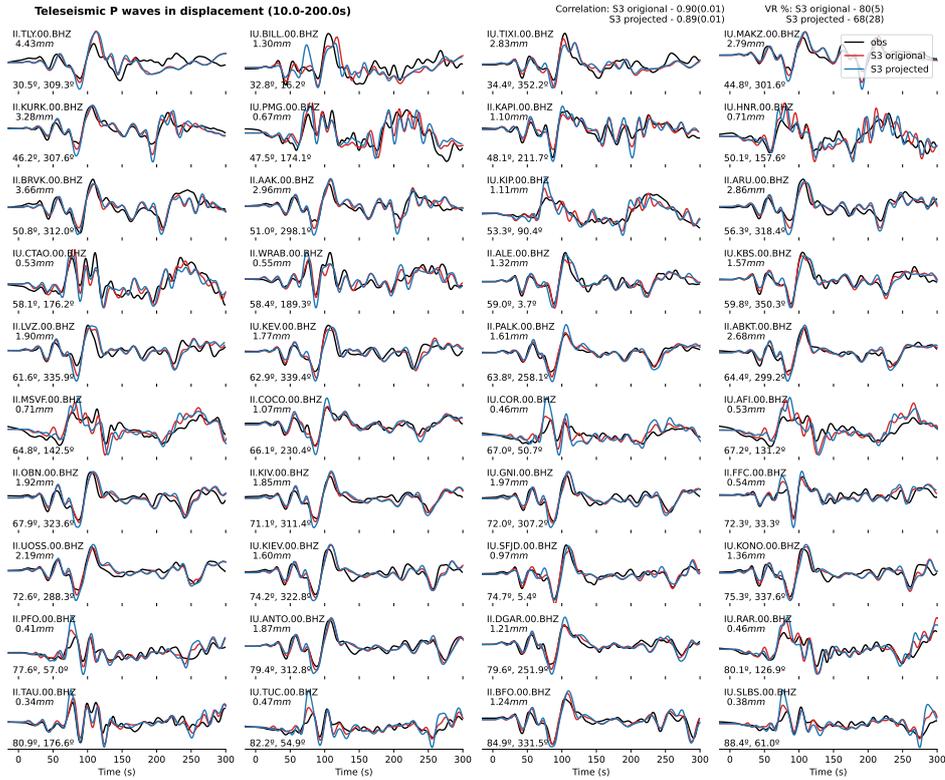


Figure S17. Comparison of the Telesismic P wave on changing fault geometry. P wave synthetics of the S3 original model (red) and S3 projected model (blue) and observations (black) for all 40 stations in Figure 11. The waveform is filtered between 10–200s period and aligned with maximum cross-correlation value. Overall correlation and variance reduction value with the observations are labeled at the top-right corner of the figure. Medians and standard deviations of the correlation value of the original model and projected model synthetics are 0.9 and 0.01, and 0.89 and 0.01, respectively. The median variance reduction of the original model is 80%, and the projected model is 68%, respectively. Distance in degree and back azimuth of the station are shown at the bottom-left corner of each waveform plot. Station trace ID and amplitude are labeled at the upper-left corner of each waveform plot.

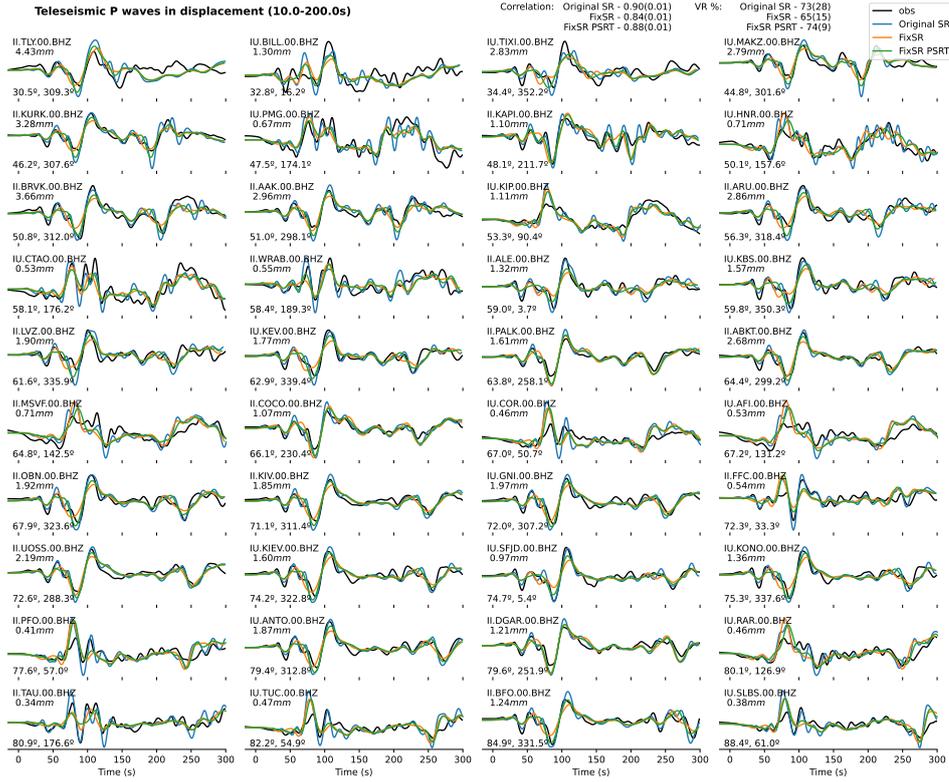


Figure S18. Comparison of the Teleseismic P wave on unifying slip rate function with Yoffe function and rupture front alignment. Same plotting as Figure S17. P wave synthetics of the S3 projected model [S3p] (blue), S3 projected unified slip rate model [S3p FixSR](orange), S3 projected unified slip rate model aligned with S3 peak slip rate time [S3p FixSR PSRT](green) and observations (black) of all 40 stations.

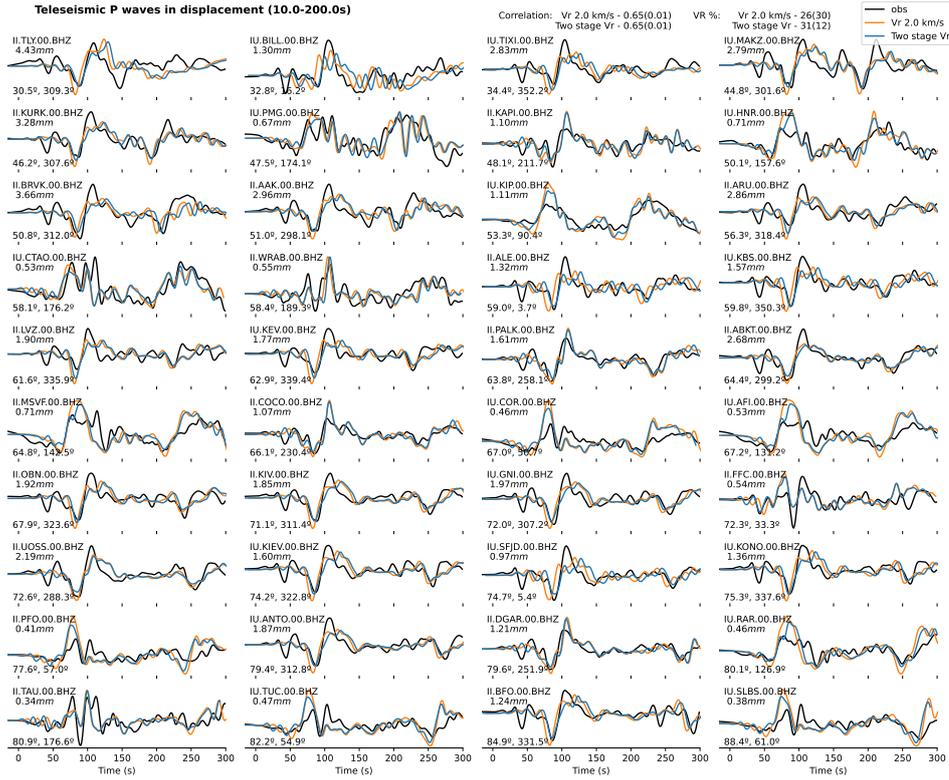


Figure S19. Comparison of the Teleseismic P wave on aligning rupture onset with constant rupture velocity. Same plotting as Figure S17. S3 projected with fix 2.0 km/s rupture velocity model [S3p Vr 20km/s](blue), P wave synthetics with two steps 1.5 km/s and 2.0 km/s rupture velocity model [orange] (blue) and observations (black) of all 40 stations.

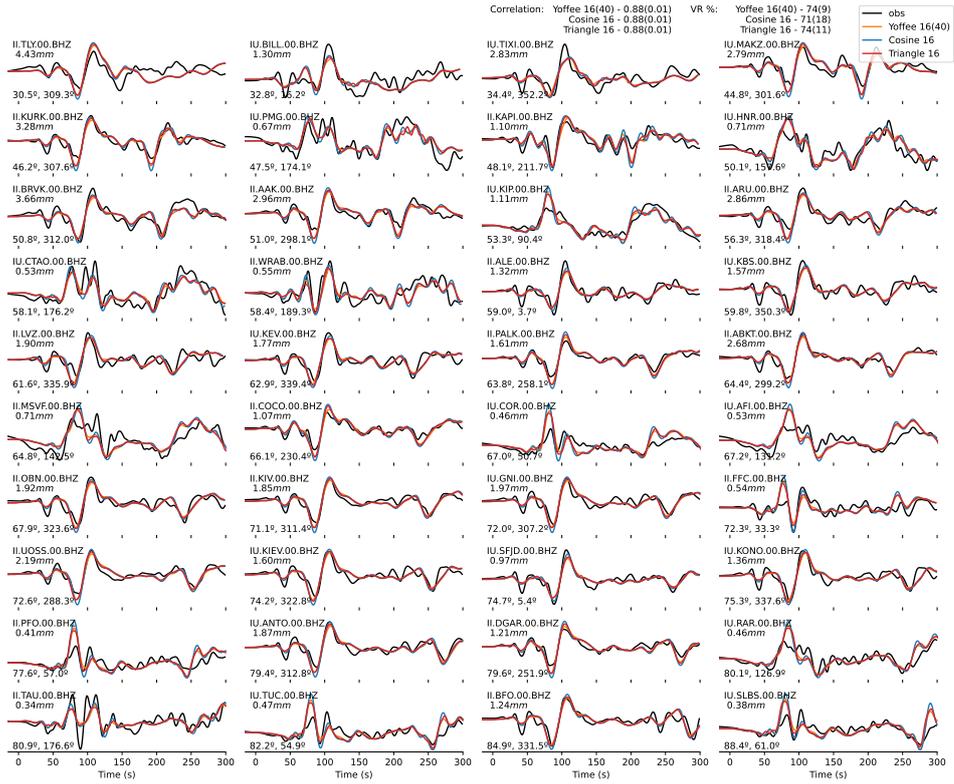


Figure S20. Comparison of the Teleseismic P wave with varying slip-rate function. Same plotting as Figure S17. P wave synthetics with Yoffe slip-rate function (orange), synthetics with cosine slip-rate function (blue), synthetics with triangular slip-rate function (red), and observations (black) of all 40 stations.

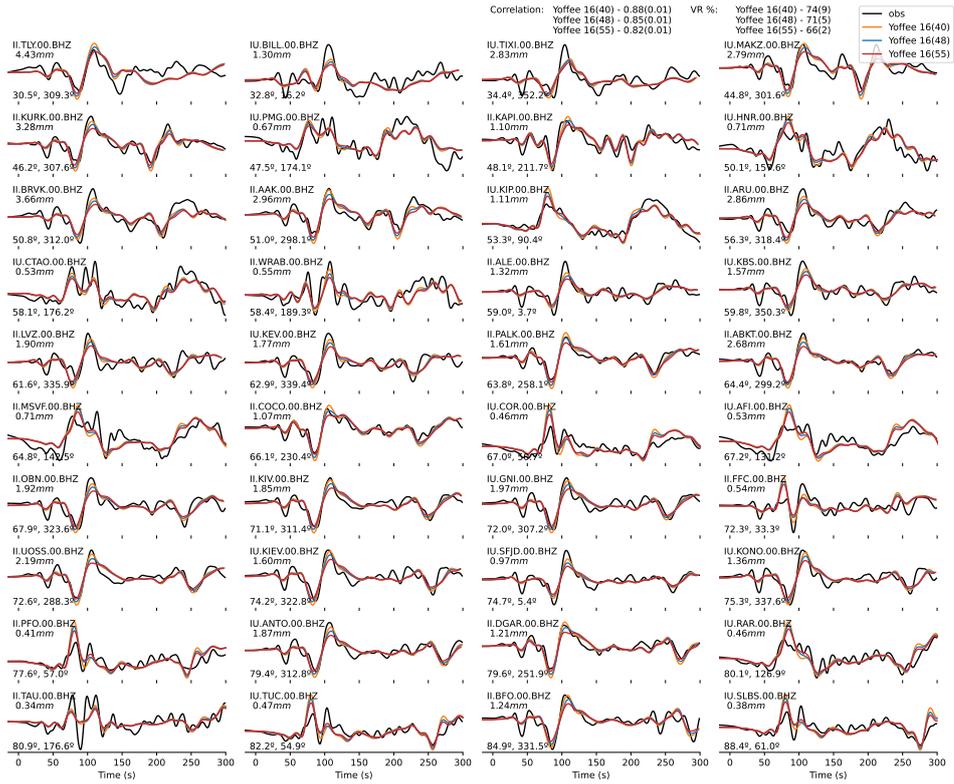


Figure S21. Comparison of the Teleseismic P wave with varying Yoffe slip-rate function. Same plotting as Figure S17. P wave synthetics with Yoffe function rise time and duration of 16 and 40 s (orange), synthetic with Yoffe function rise time and duration of 16 and 48s (blue), synthetics with Yoffe function rise time and duration of 16 and 55s (red), and observations (black) of all 40 stations.

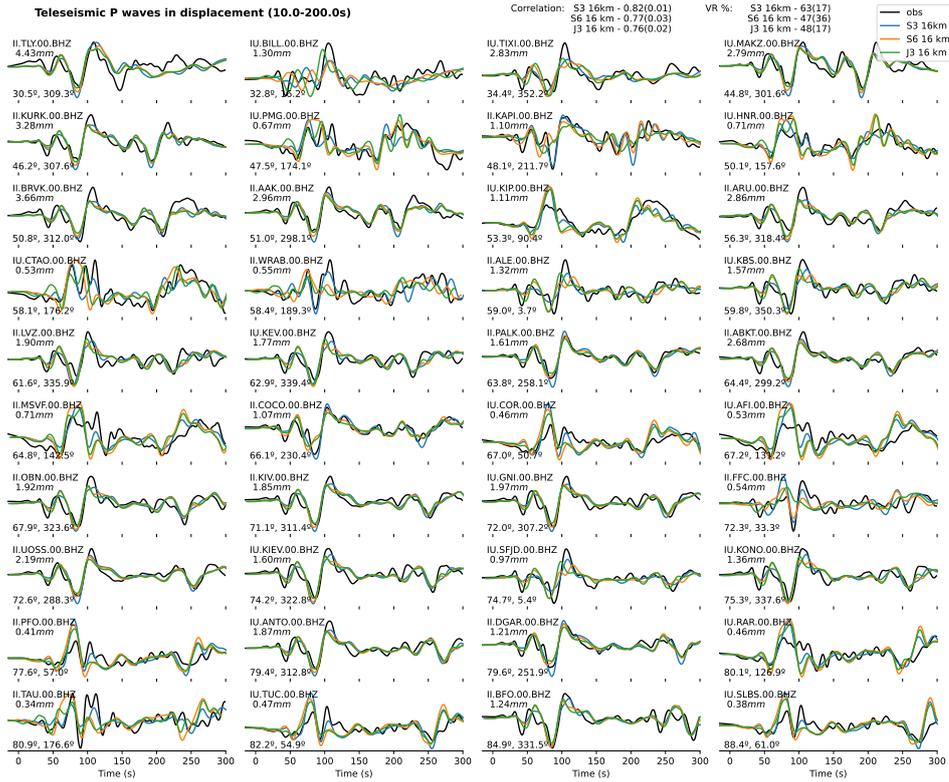


Figure S22. Comparison of the Teleseismic P wave with slip model S3, S6 and J3 at 16 km resolution. Same plotting as Figure S17. P wave synthetics of slip model S3 (blue), synthetics of slip model S6 (orange), synthetics of slip model J3 (green), and observations (black) of all 40 stations.

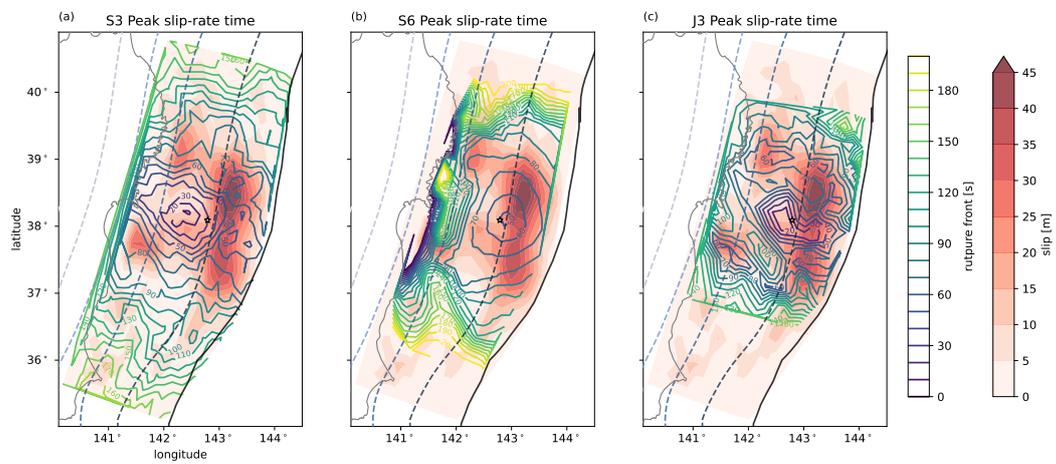


Figure S23. Comparing models peak slip-rate time. Color contours show the (a) S3, (b) S6, and (c) J3 models' peak slip-rate time, respectively. Model S3 slip distribution is shown as the color-filled contour. The peak slip-rate time of models S6 and J3 are spatially limited due to the different fault parameterization of these two models. Hypocenters of these models are also shifted due to the projection onto the realistic geometry

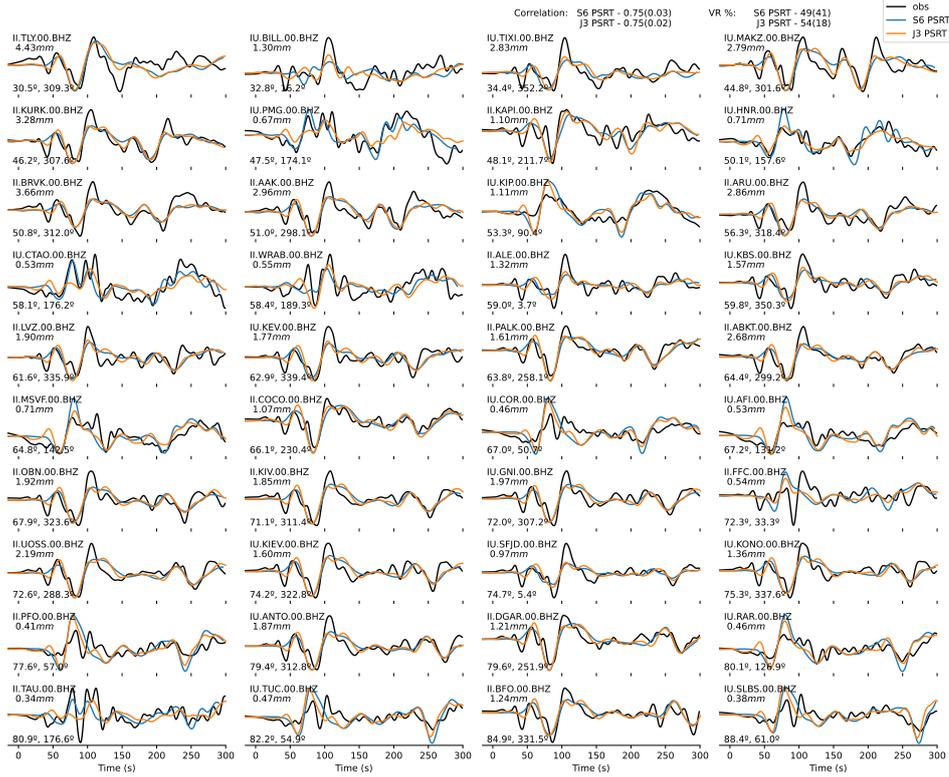


Figure S24. Comparison of the Teleseismic P wave with rupture front alignment with the peak-slip-rate time of S6 and J3 models with S3 slip model at 16 km resolution. Same plotting as Figure S17. P wave synthetics with rupture front align with S6 peak-slip-rate time (blue), synthetics with rupture front align with J3 peak-slip-rate time (orange), and observations (black) of all 40 stations.

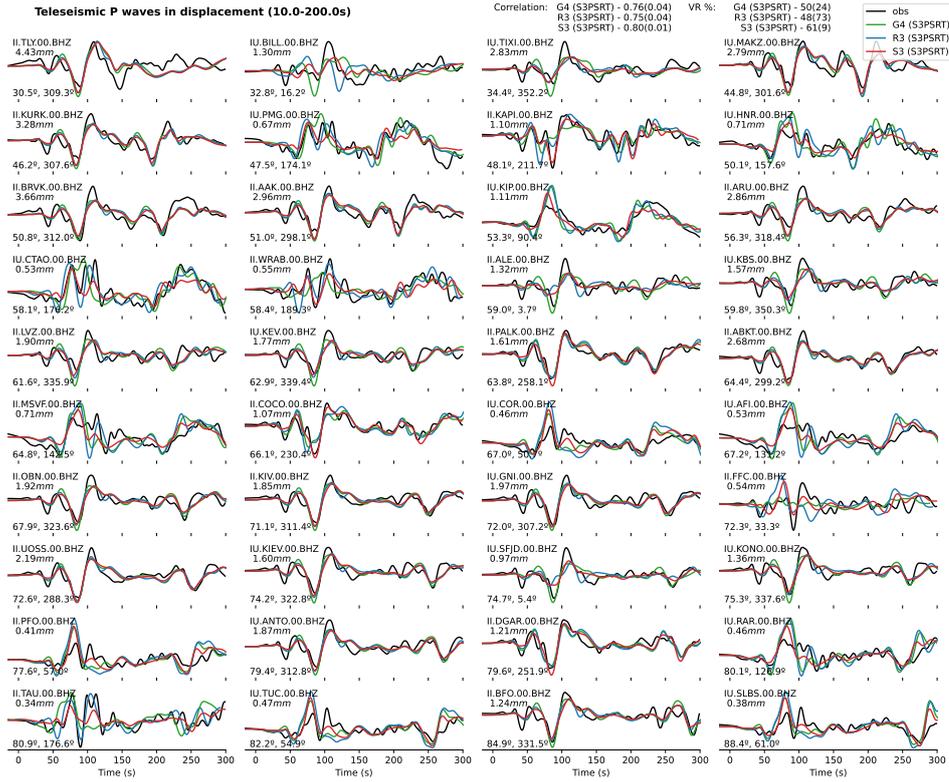


Figure S25. Comparison of the Teleseismic P wave with slip model G4, R3 and S3 at 16 km resolution. Same plotting as Figure S17. P wave synthetics with G4 model slip distribution (green), synthetics with R3 model slip distribution (blue), synthetics with S3 model slip distribution (red), and observations (black) of all 40 stations.

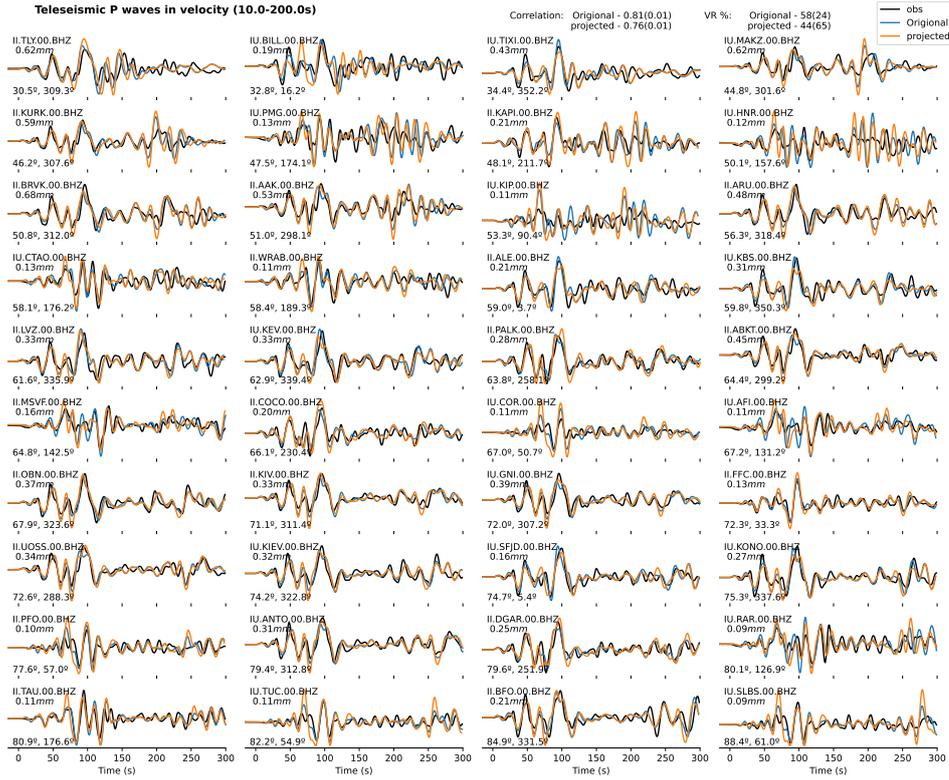


Figure S26. Comparison of the Teleseismic velocity P wave with original S3 finite-fault model and projected S3 finite-fault model. Same plotting as Figure S17. P wave synthetics of the original S3 finite-fault model (blue), synthetics of the projected S3 finite-fault model (orange), and observations (black) of all 40 stations.

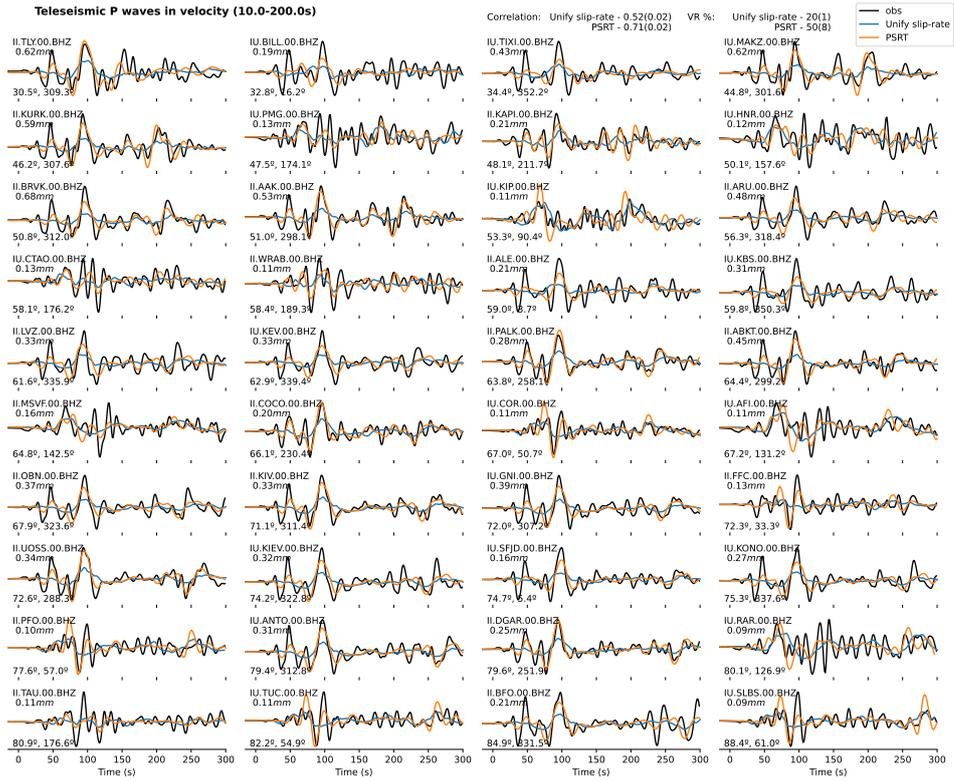


Figure S27. Comparison of the Teleseismic velocity P wave with unified slip-rate function with original onset-time alignment and peak-slip-rate time alignment. Same plotting as Figure S17. P wave synthetics of unified slip-rate function with original onset-time alignment (blue), synthetics of unified slip-rate function with peak-slip-rate time alignment (orange), observations (black) of all 40 stations.

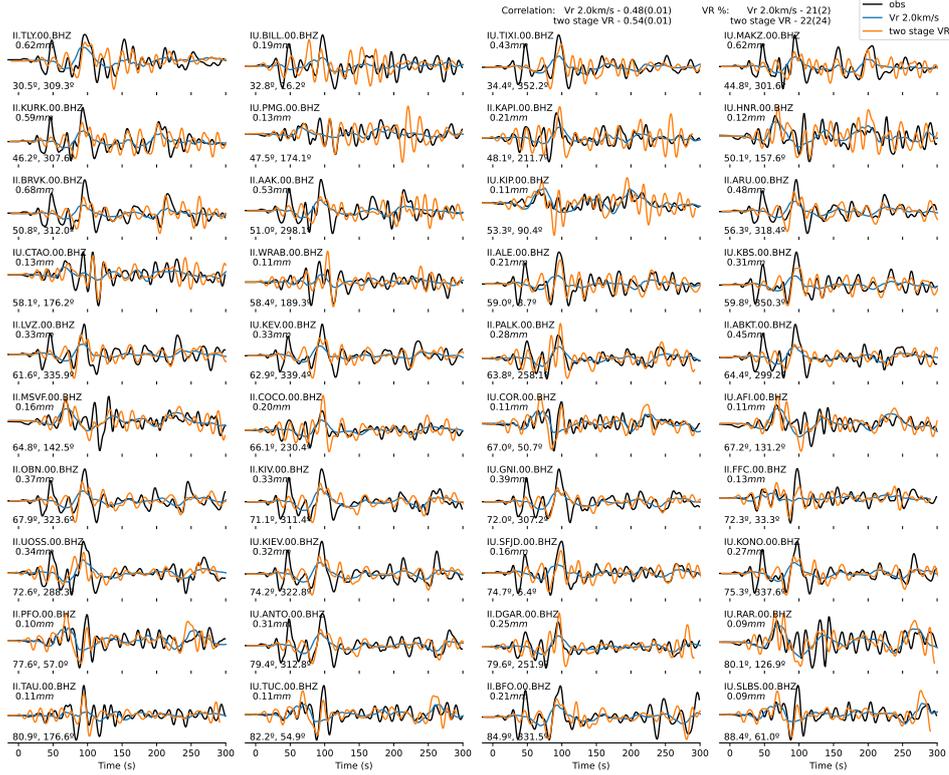


Figure S28. Comparison of the Teleseismic velocity P wave with onset-time alignment with constant rupture speed of 2.0 km/s and two-step rupture speed with S3 slip distribution. Same plotting as Figure S17. P wave synthetics of constant rupture speed of 2.0 km/s (blue), synthetics of two-step rupture speed (orange), observations (black) of all 40 stations.

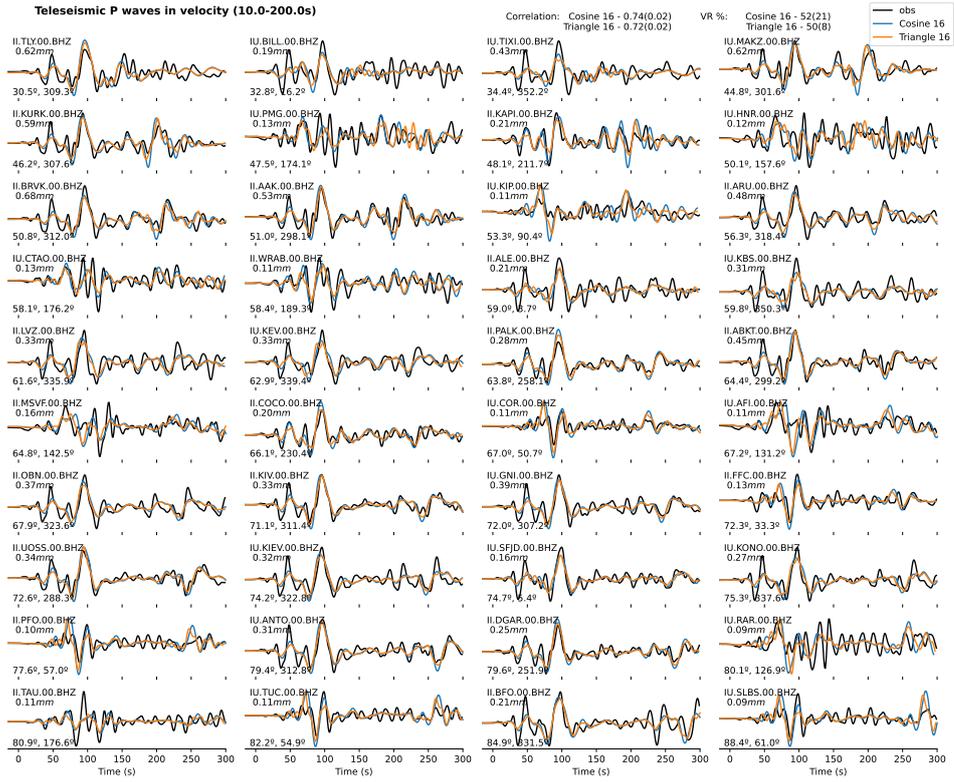


Figure S29. Comparison of the Teleseismic velocity P wave with cosine slip-rate function and triangular slip-rate function. Same plotting as Figure S17. P wave synthetics of cosine slip-rate function (blue), synthetics of triangle slip-rate function (orange), observations (black) of all 40 stations.

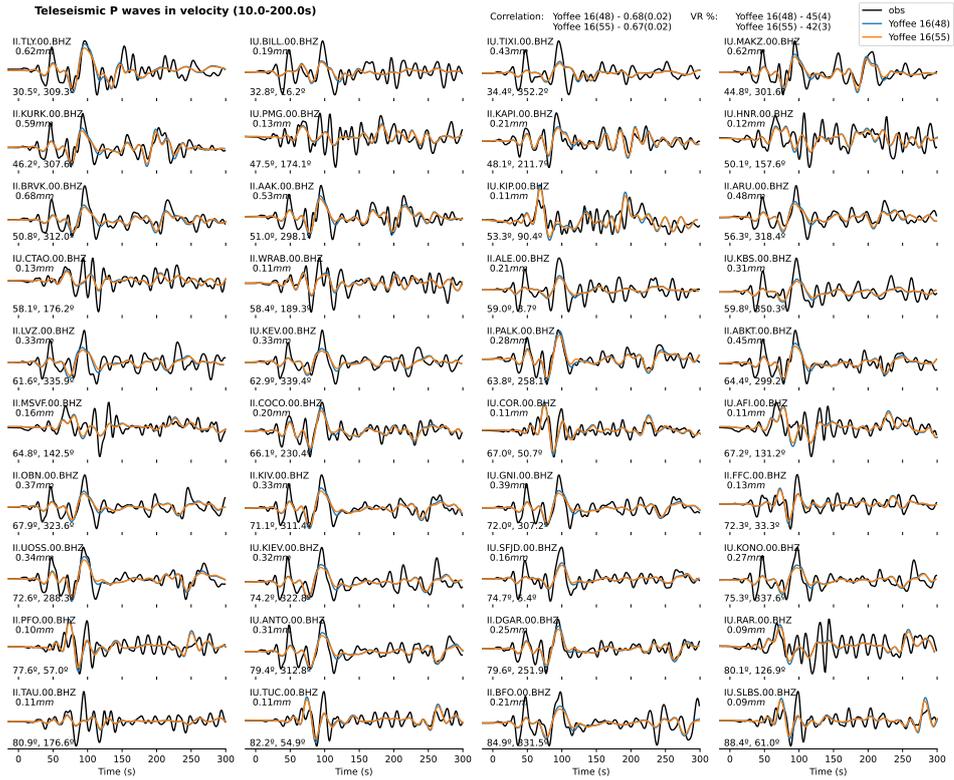


Figure S30. Comparison of the Teleseismic velocity P wave with varying Yoffe function. Same plotting as Figure S17. P wave synthetics of the Yoffe function with 48s duration (blue), synthetics of the Yoffe function with 55s duration (orange), and observations (black) of all 40 stations.

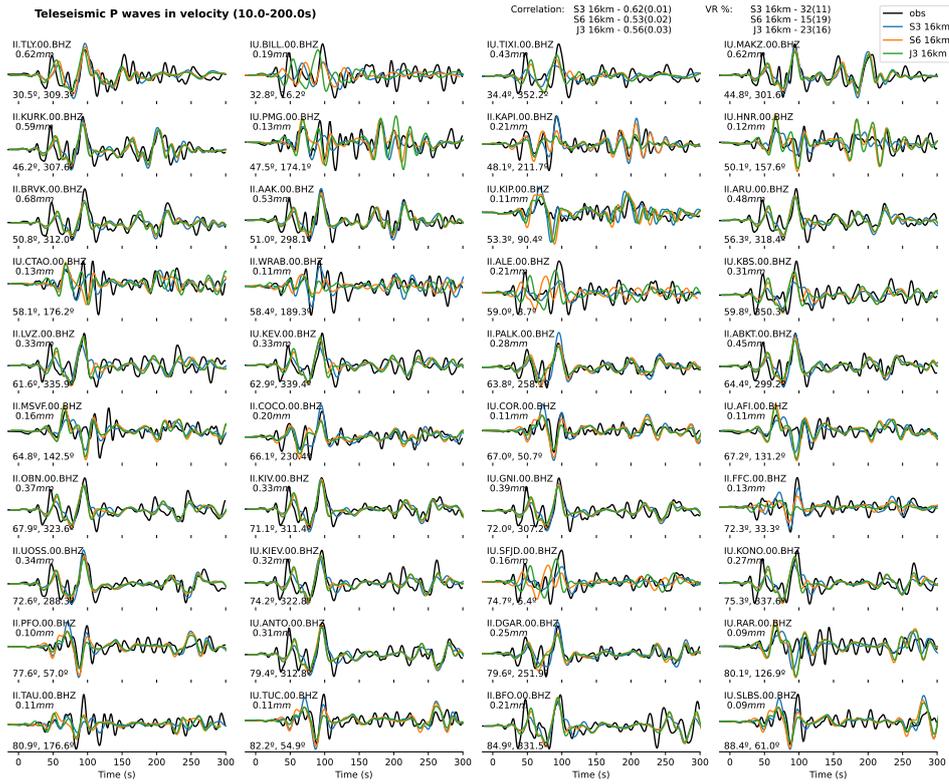


Figure S31. Comparison of the Teleseismic velocity P wave with different model slip distribution and S3 model PSRT onset-time alignment. Same plotting as Figure S17. P wave synthetics of S3 slip model (blue), synthetics of S6 slip model (orange), synthetics of J3 slip model (green), and observations (black) of all 40 stations.

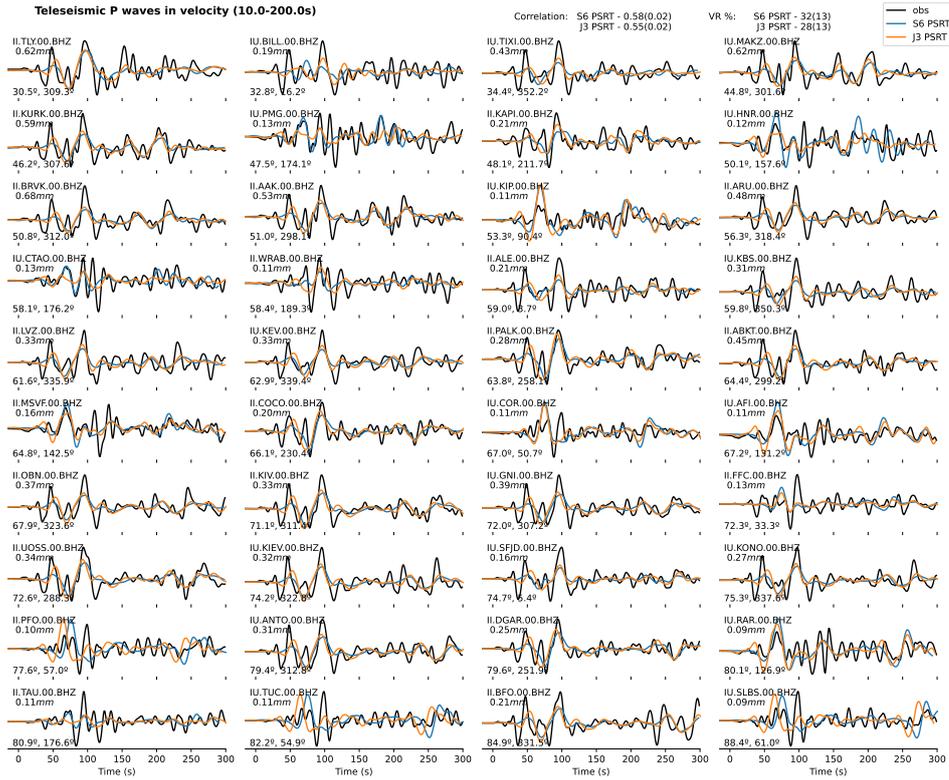


Figure S32. Comparison of the Teleseismic velocity P wave with different model PSRT onset-time alignment and S3 model slip distribution. Same plotting as Figure S17. P wave synthetics of S6 model PSRT (blue), synthetics of J3 model PSRT (orange), and observations (black) of all 40 stations.

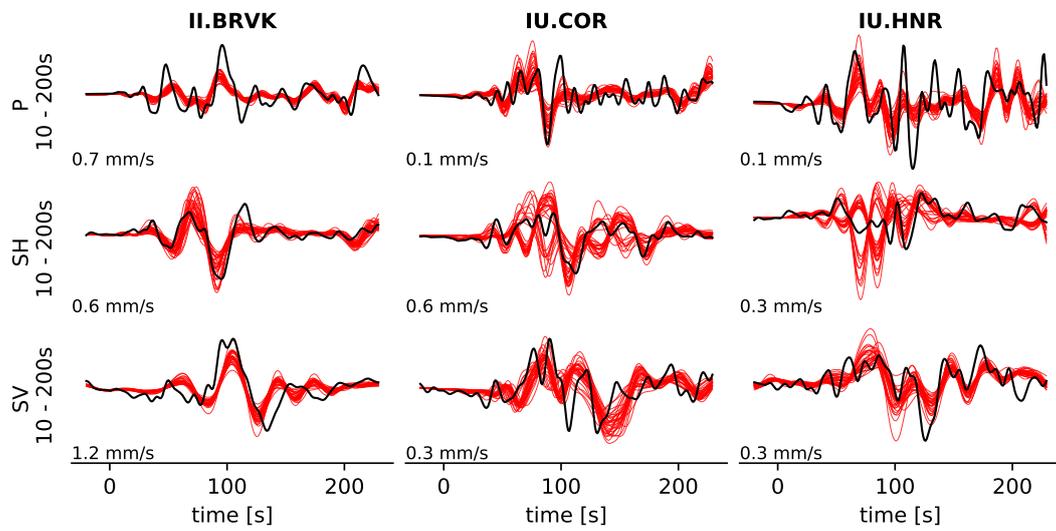


Figure S33. Comparison of teleseismic velocity observations and synthetics at a 16 km scale. Synthetic and observed teleseismic waveforms. Black lines are the observed waveforms; red lines are the synthetic waveforms from the 32 finite-fault models and the median model. Three rows are P wave, SH wave and SV wave, respectively. Amplitudes of the observed waveforms are labeled at the lower-left corner of each waveform plot.

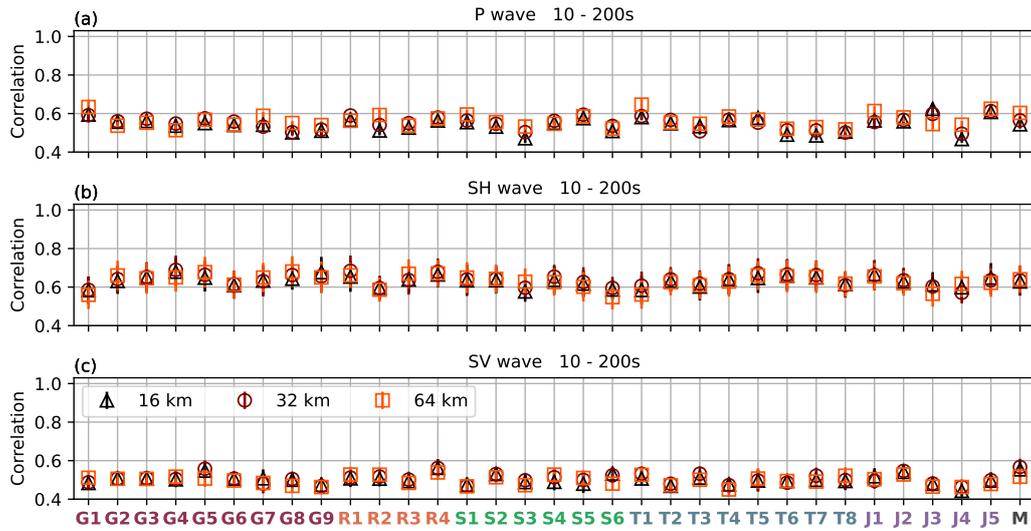


Figure S34. Correlation coefficient values between the teleseismic velocity observations and synthetics at the 16, 32, and 64 km scales. (a) P wave. (b) SH wave. (c) SV wave. Median correlation values between the synthetic and observed teleseismic waveforms at the 40 teleseismic stations are taken as the characteristic correlation coefficient values for each model. Three markers indicate the characteristic median values for models at the 16, 32, and 64 km scales. Error bars represent the associated standard deviation of correlation coefficient values of the 40 stations.

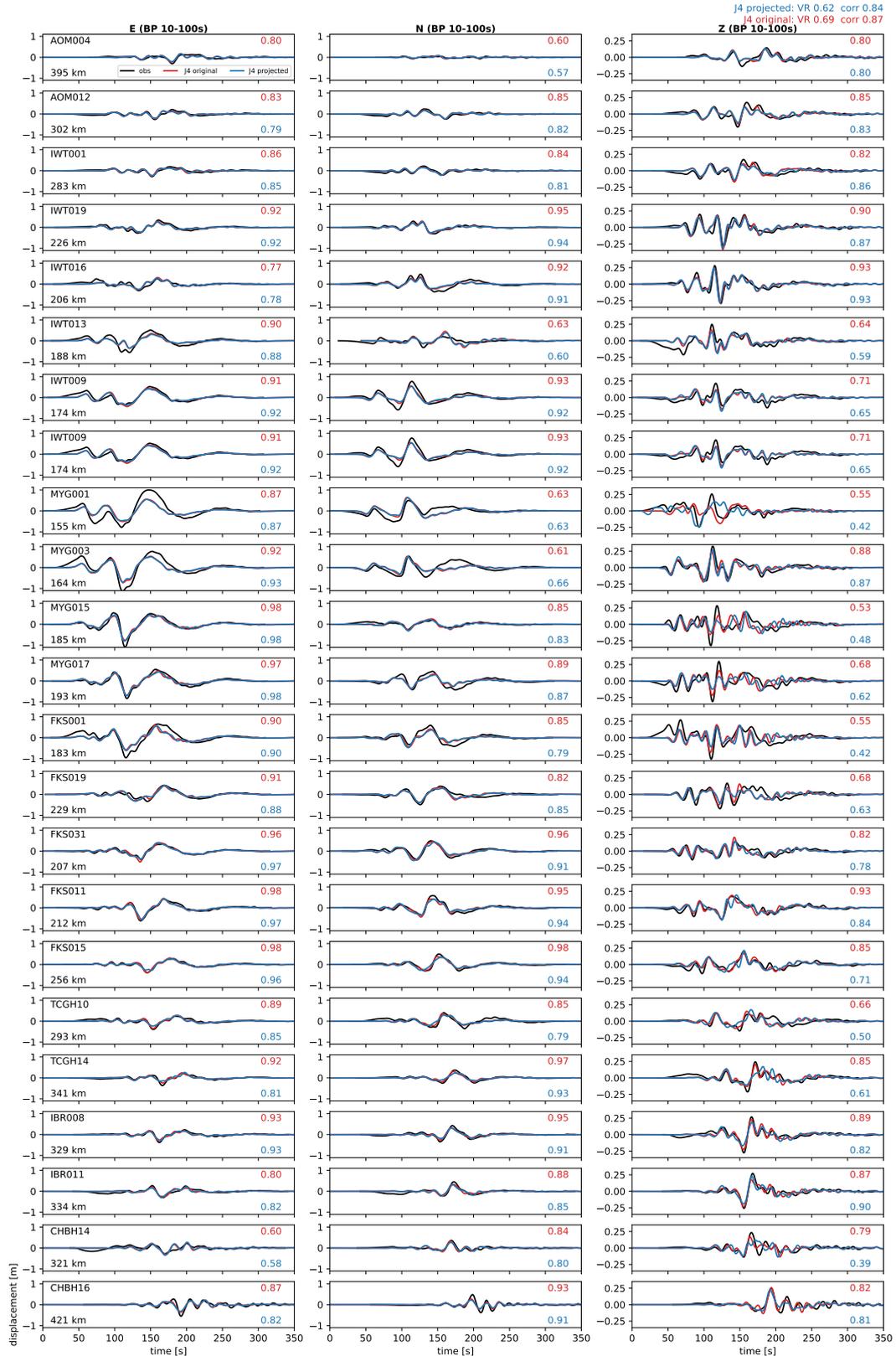


Figure S35. Comparison of strong ground motion observations and synthetics of original and projected J4 model. Black lines are the observations. Red lines are the synthetics from J4 original subfault geometry. Blue lines are the synthetics with the projected J4 model. The correlation values of each component are shown on the top right and bottom right of each waveform subplot. Station name and distance from the centroid location are shown in top left and bottom left of each waveform subplot. The overall median variance and the correlation value of the two sets of synthetics are shown at the top right of the figure.

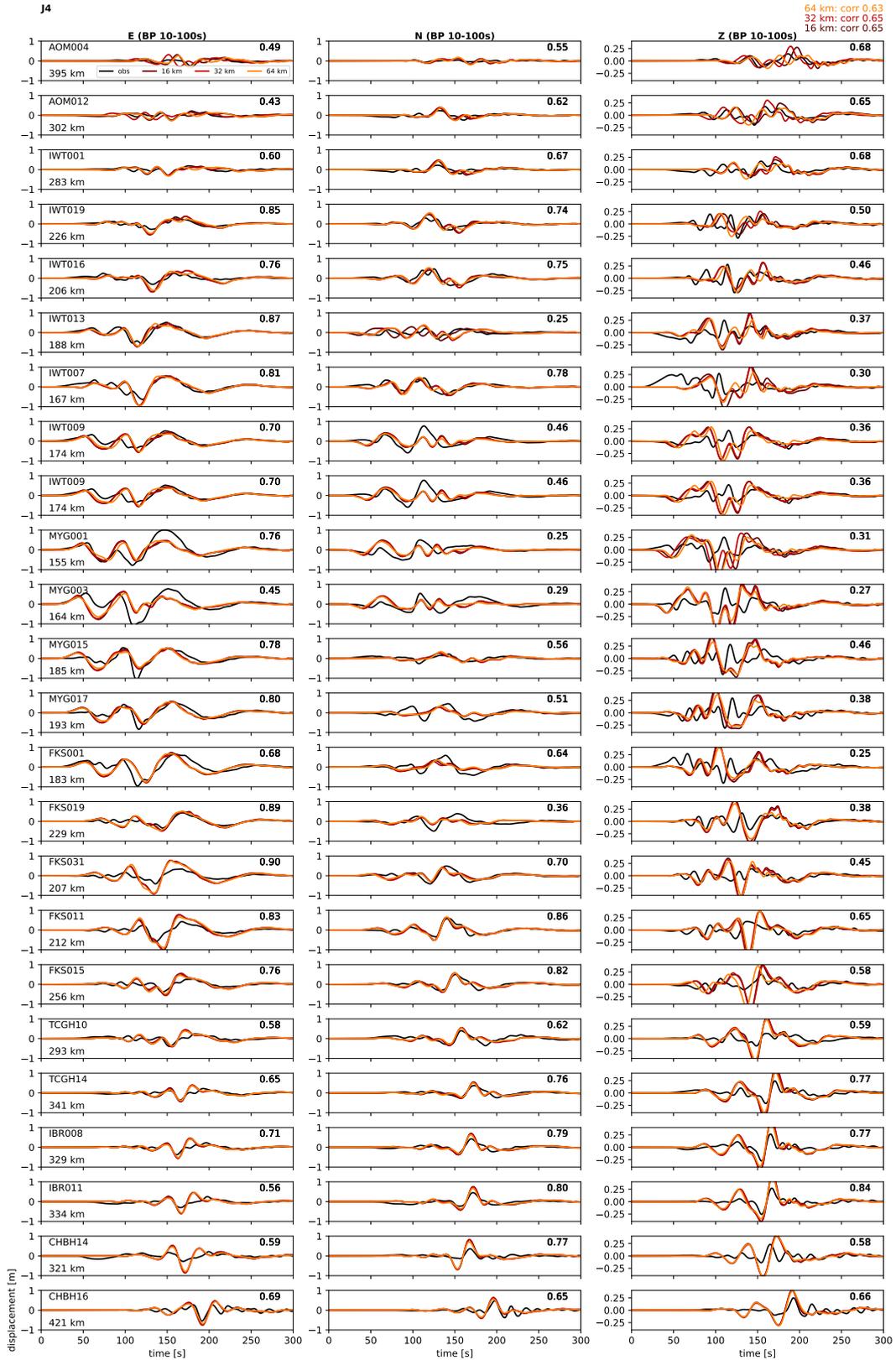


Figure S36. Comparison of strong ground motion observations and synthetics of projected and unified slip-rate J4 model at 16, 32 and 64 km scale. Black lines are the observations. Dark red, red, and yellow lines are the J4 synthetics of 16, 32, and 64 km scale, respectively. The correlation values of each component are shown on the top right and bottom right of each waveform subplot. Station name and distance from the centroid location are shown in top left and bottom left of each waveform subplot. The overall median variance and the correlation value of the two sets of synthetics are shown at the top right of the figure.

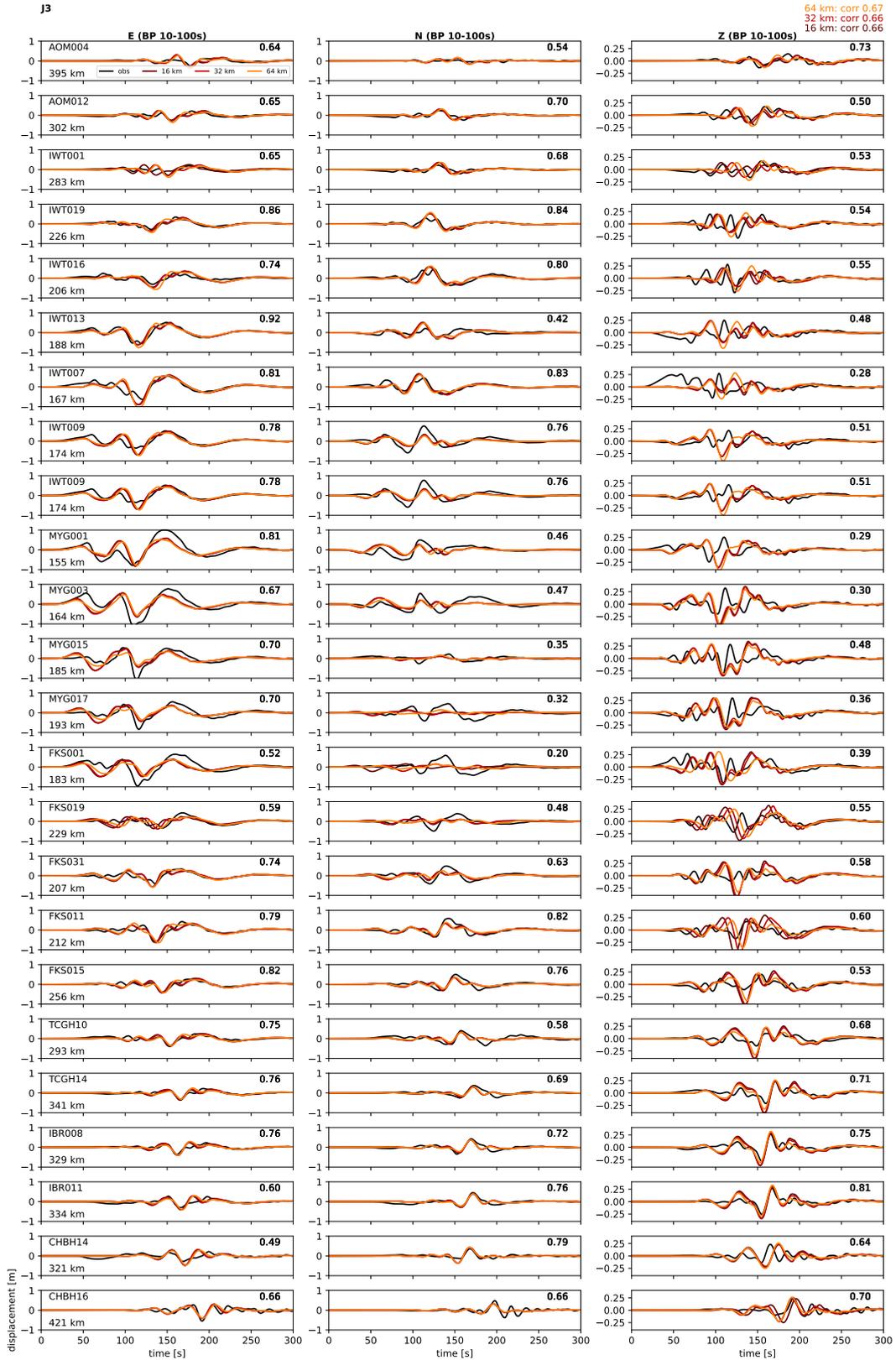


Figure S37. Comparison of strong ground motion observations and synthetics of projected and unified slip-rate J3 model at 16, 32 and 64 km scale. Black lines are the observations. Dark red, red, and yellow lines are the J4 synthetics of 16, 32, and 64 km scale, respectively. The correlation values of each component are shown on the top right and bottom right of each waveform subplot. Station name and distance from the centroid location are shown in top left and bottom left of each waveform subplot. The overall median variance and the correlation value of the two sets of synthetics are shown at the top right of the figure.

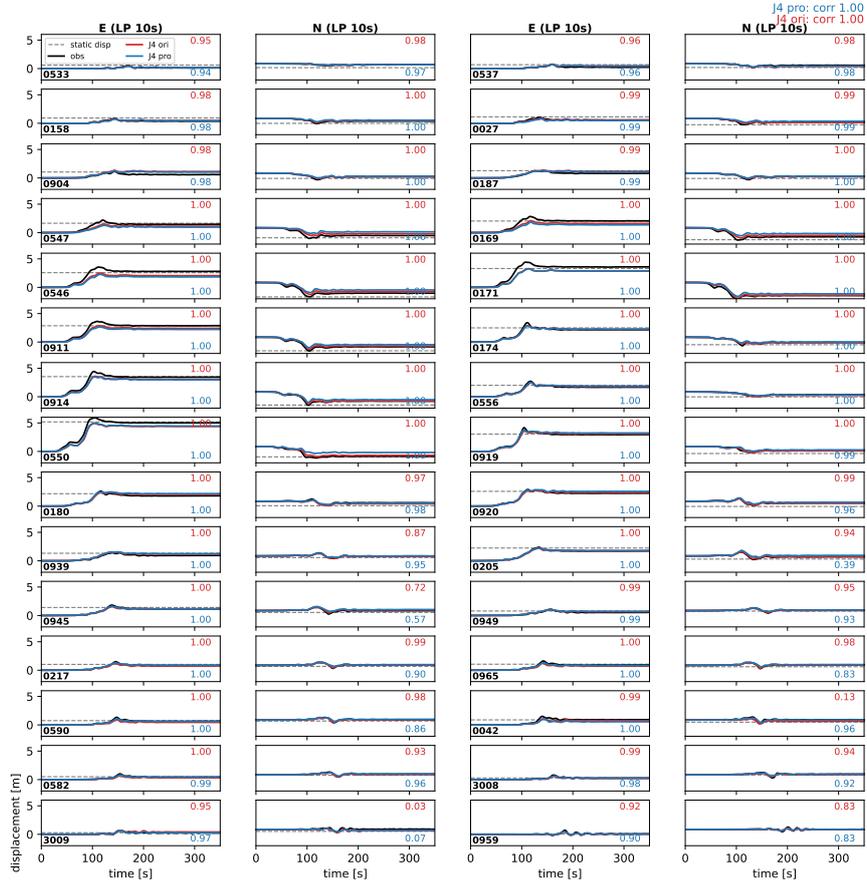


Figure S38. Comparison of high rate-GNSS observations and synthetics of original and projected J4 model. Black lines are the observations. Red and blue lines are the J4 synthetics of the original finite-fault model and the projected model. The grey dashed line is the static offset using the 3D velocity structure Green’s function. The correlation values of each component are shown on the top right and bottom right of each waveform subplot. Station name and distance from the centroid location are shown in top left and bottom left of each waveform subplot. The overall median variance and the correlation value of the two sets of synthetics are shown at the top right of the figure.

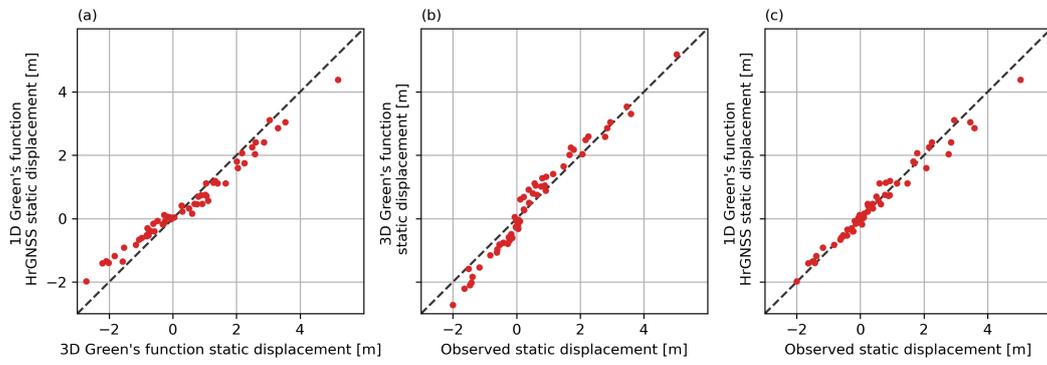


Figure S39. Comparison of static offset between Model J4 HrGNSS synthetics using 1D Green's function, Model J4 static offset synthetics using 3D Green's function and observations.

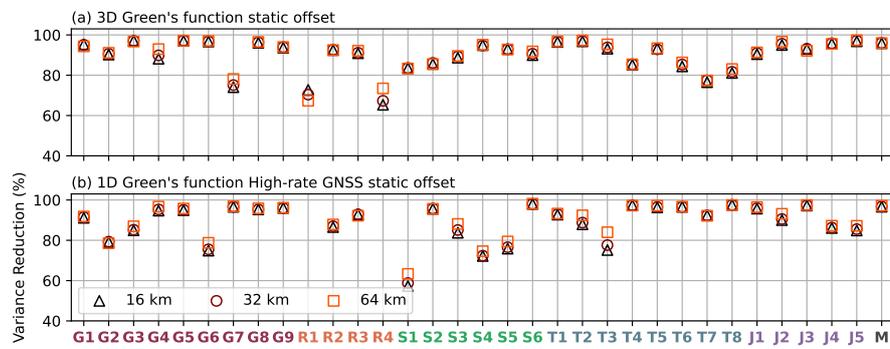


Figure S40. Geodetic offset variance reduction comparison with (a) 3D Green's function and (b) 1D Green's function High-rate GNSS static offset with the observations for 33 models at 16, 32, and 64 km scale. Markers indicate the variance reduction of the static offset between the synthetics and the observations.

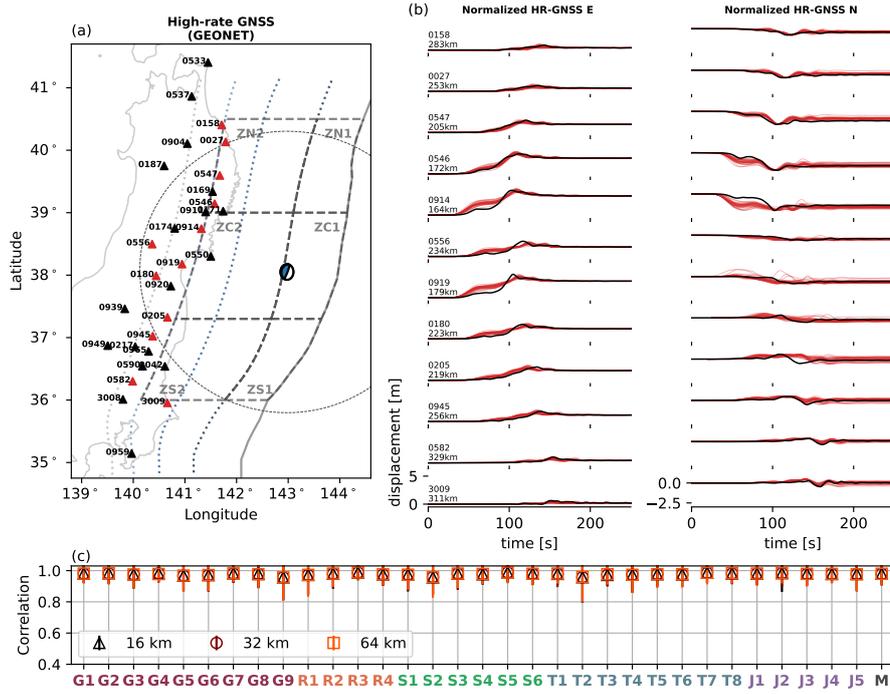


Figure S41. Comparison of normalized high-rate GNSS observations and synthetics at 16 km slip model scale. (a) Map view of the GEONET stations used in the study. Red triangles are the stations in (b). Beach-ball focal mechanism represents the centroid location of the median model. Dotted circles show the centroid distance of 250 km. (b) Black lines are the observed waveforms; Red lines are the synthetics from the 32 finite-fault models and the median model at the 16 km scale, with their amplitude normalized with the observed amplitude. (c) Correlation coefficient values between the observations and synthetics at the 16, 32, and 64 km scale. Markers indicate the median correlation values of all stations, with an error bar indicating the associated standard deviation.

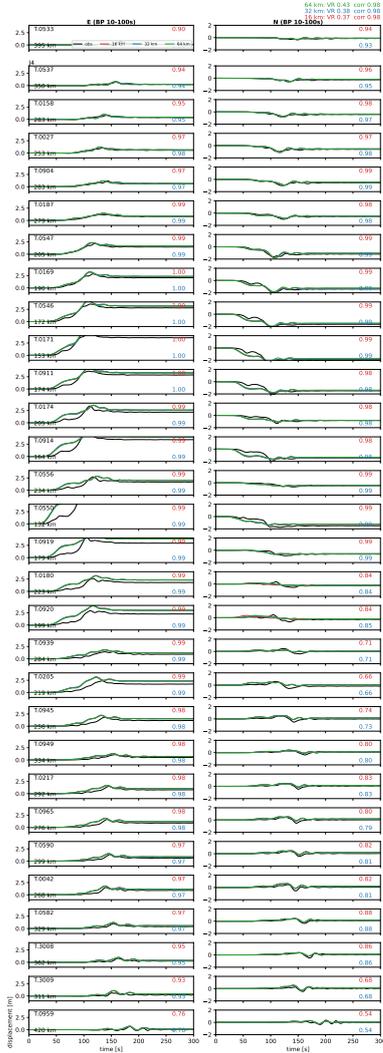


Figure S42. Comparison of high rate-GNSS observations and synthetics of projected and unified slip-rate J4 model at 16, 32 and 64 km scale. Black lines are the observations. Dark red, red, and yellow lines are the J4 synthetics of 16, 32, and 64 km scale, respectively. The correlation values of each component are shown on the top right and bottom right of each waveform subplot. Station name and distance from the centroid location are shown in top left and bottom left of each waveform subplot. The overall median variance and the correlation value of the two sets of synthetics are shown at the top right of the figure.

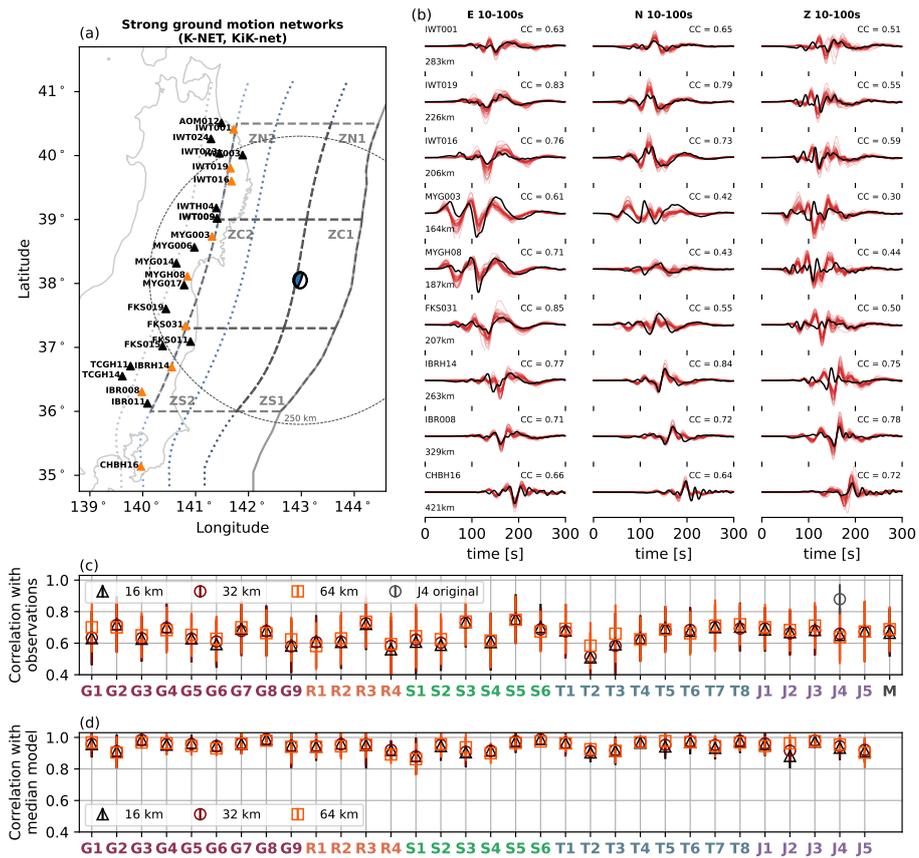


Figure S43. Comparison of regional strong-ground motion records (displacement) with synthetics at 32 km slip model scale. Same plotting style with Figure 14.

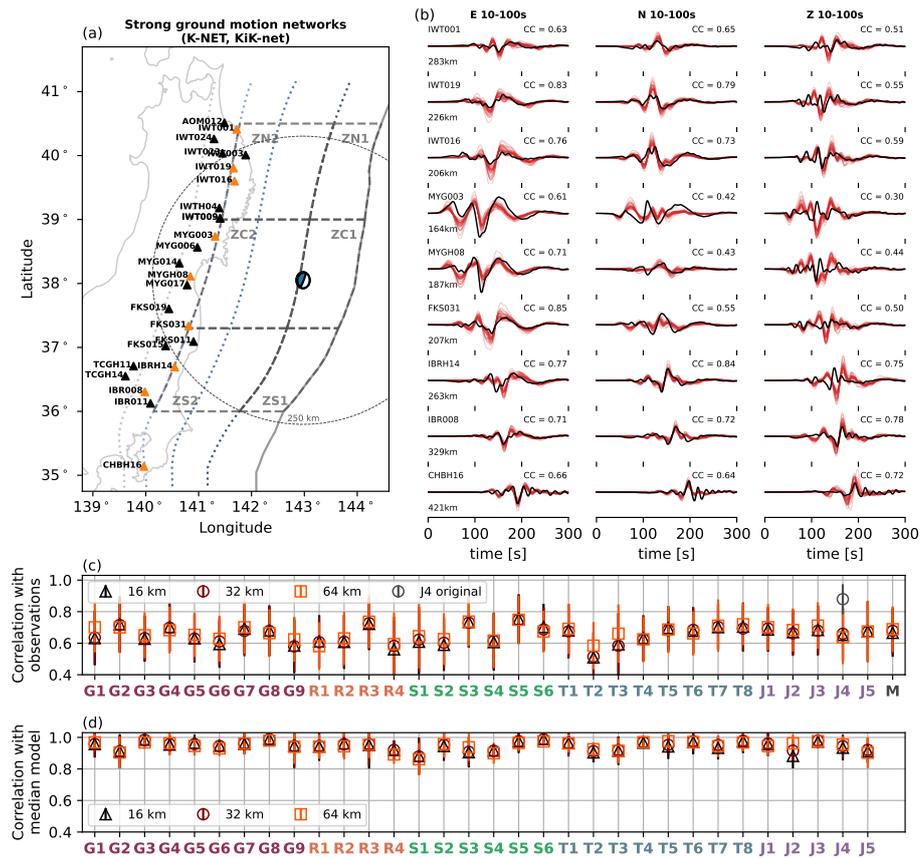


Figure S44. Comparison of regional strong-ground motion records (displacement) with synthetics at 64 km slip model scale. Same plotting style with Figure 14.

385 **References**

- 386 Ammon, C. J., Lay, T., Kanamori, H., & Cleveland, M. (2011). A rupture model of
 387 the 2011 off the Pacific coast of Tohoku earthquake. *Earth, Planets and Space*,
 388 *63*(7), 693–696.
- 389 Bletery, Q., Sladen, A., Delouis, B., Vallée, M., Nocquet, J.-M., Rolland, L., &
 390 Jiang, J. (2014). A detailed source model for the M_w 9.0 Tohoku-Oki earth-
 391 quake reconciling geodesy, seismology, and tsunami records. *Journal of Geo-*
 392 *physical Research: Solid Earth*, *119*(10), 7636–7653.
- 393 Diao, F., Xiong, X., & Zheng, Y. (2012). Static slip model of the m_w 9.0 Tohoku
 394 (Japan) earthquake: Results from joint inversion of terrestrial GPS data and
 395 seafloor GPS/acoustic data. *Chinese Science Bulletin*, *57*, 1990–1997.
- 396 Dziewonski, A. M., & Anderson, D. L. (1981). Preliminary reference earth model.
 397 *Physics of the earth and planetary interiors*, *25*(4), 297–356.
- 398 Fujii, Y., Satake, K., Sakai, S., Shinohara, M., & Kanazawa, T. (2011). Tsunami
 399 source of the 2011 off the Pacific coast of Tohoku earthquake. *Earth, planets*
 400 *and space*, *63*(7), 815–820.
- 401 Goldberg, D., Barnhart, W., & Crowell, B. (2022). Regional and teleseismic observa-
 402 tions for finite-fault product. *US Geol. Surv. Data Release*.
- 403 Gusman, A. R., Tanioka, Y., Sakai, S., & Tsushima, H. (2012). Source model of the
 404 great 2011 Tohoku earthquake estimated from tsunami waveforms and crustal
 405 deformation data. *Earth and Planetary Science Letters*, *341*, 234–242.
- 406 Hashima, A., Becker, T. W., Freed, A. M., Sato, H., & Okaya, D. A. (2016). Co-
 407 seismic deformation due to the 2011 Tohoku-Oki earthquake: influence of 3-D
 408 elastic structure around Japan. *Earth, Planets and Space*, *68*(1), 1–15.
- 409 Hayes, G. P. (2011, 09). Rapid source characterization of the 2011 M_w 9.0 off the
 410 Pacific coast of Tohoku earthquake. *Earth, Planets and Space*, *63*(7), 529–534.
- 411 Hooper, A., Pietrzak, J., Simons, W., Cui, H., Riva, R., Naeije, M., ... Socquet, A.
 412 (2013). Importance of horizontal seafloor motion on tsunami height for the
 413 2011 $M_w=9.0$ Tohoku-Oki earthquake. *Earth and Planetary Science Letters*,
 414 *361*, 469–479.
- 415 Ide, S., Baltay, A., & Beroza, G. C. (2011). Shallow dynamic overshoot and ener-
 416 getic deep rupture in the 2011 M_w 9.0 Tohoku-Oki earthquake. *Science*,
 417 *332*(6036), 1426–1429.
- 418 Iinuma, T., Hino, R., Kido, M., Inazu, D., Osada, Y., Ito, Y., ... others (2012). Co-
 419 seismic slip distribution of the 2011 off the Pacific Coast of Tohoku earthquake
 420 ($M9.0$) refined by means of seafloor geodetic data. *Journal of Geophysical*
 421 *Research: Solid Earth*, *117*(B7).
- 422 Ito, T., Ozawa, K., Watanabe, T., & Sagiya, T. (2011). Slip distribution of the 2011
 423 off the Pacific coast of Tohoku earthquake inferred from geodetic data. *Earth,*
 424 *planets and space*, *63*(7), 627–630.
- 425 Jiang, J., & Simons, M. (2016). Probabilistic imaging of tsunamigenic seafloor de-
 426 formation during the 2011 Tohoku-Oki earthquake. *Journal of Geophysical Re-*
 427 *search: Solid Earth*, *121*(12), 9050–9076.
- 428 Kubo, H., & Kakehi, Y. (2013). Source process of the 2011 Tohoku earthquake
 429 estimated from the joint inversion of teleseismic body waves and geodetic data
 430 including seafloor observation data: source model with enhanced reliability by
 431 using objectively determined inversion settings. *Bulletin of the Seismological*
 432 *Society of America*, *103*(2B), 1195–1220.
- 433 Kubota, T., Saito, T., & Hino, R. (2022). A new mechanical perspective on a shal-
 434 low megathrust near-trench slip from the high-resolution fault model of the
 435 2011 Tohoku-Oki earthquake. *Progress in Earth and Planetary Science*, *9*(1),
 436 1–19.
- 437 Lee, S.-J., Huang, B.-S., Ando, M., Chiu, H.-C., & Wang, J.-H. (2011). Evidence of
 438 large scale repeating slip during the 2011 Tohoku-Oki earthquake. *Geophysical*
 439 *Research Letters*, *38*(19).

- 440 Melgar, D., & Bock, Y. (2015). Kinematic earthquake source inversion and tsunami
441 runup prediction with regional geophysical data. *Journal of Geophysical Re-*
442 *search: Solid Earth*, *120*(5), 3324–3349.
- 443 Minson, S. E., Simons, M., Beck, J., Ortega, F., Jiang, J., Owen, S., ... Sladen, A.
444 (2014). Bayesian inversion for finite fault earthquake source models—ii: the
445 2011 great Tohoku-Oki, Japan earthquake. *Geophysical Journal International*,
446 *198*(2), 922–940.
- 447 Nissen-Meyer, T., van Driel, M., Stähler, S. C., Hosseini, K., Hempel, S., Auer,
448 L., ... Fournier, A. (2014). AxiSEM: broadband 3-D seismic wavefields in
449 axisymmetric media. *Solid Earth*, *5*(1), 425–445.
- 450 Pollitz, F. F., Bürgmann, R., & Banerjee, P. (2011). Geodetic slip model of the 2011
451 M9.0 Tohoku earthquake. *Geophysical Research Letters*, *38*(7).
- 452 Romano, F., Trasatti, E., Lorito, S., Piomallo, C., Piatanesi, A., Ito, Y., ... Cocco,
453 M. (2014). Structural control on the Tohoku earthquake rupture process in-
454 vestigated by 3d FEM, tsunami and geodetic data. *Scientific reports*, *4*(1),
455 1–11.
- 456 Saito, T., Ito, Y., Inazu, D., & Hino, R. (2011). Tsunami source of the 2011
457 Tohoku-Oki earthquake, Japan: Inversion analysis based on dispersive tsunami
458 simulations. *Geophysical Research Letters*, *38*(7).
- 459 Satake, K., Fujii, Y., Harada, T., & Namegaya, Y. (2013). Time and space distribu-
460 tion of coseismic slip of the 2011 Tohoku earthquake as inferred from tsunami
461 waveform data. *Bulletin of the seismological society of America*, *103*(2B),
462 1473–1492.
- 463 Simons, M., Minson, S. E., Sladen, A., Ortega, F., Jiang, J., Owen, S. E., ... oth-
464 ers (2011). The 2011 magnitude 9.0 Tohoku-Oki earthquake: Mosaicking the
465 megathrust from seconds to centuries. *science*, *332*(6036), 1421–1425.
- 466 Suzuki, W., Aoi, S., Sekiguchi, H., & Kunugi, T. (2011). Rupture process of the
467 2011 Tohoku-Oki mega-thrust earthquake (M9. 0) inverted from strong-motion
468 data. *Geophysical Research Letters*, *38*(7).
- 469 van Driel, M., Krischer, L., Stähler, S. C., Hosseini, K., & Nissen-Meyer, T. (2015).
470 Instaseis: Instant global seismograms based on a broadband waveform
471 database. *Solid Earth*, *6*(2), 701–717.
- 472 Wang, C., Ding, X., Shan, X., Zhang, L., & Jiang, M. (2012). Slip distribution of
473 the 2011 Tohoku earthquake derived from joint inversion of GPS, InSAR and
474 seafloor GPS/acoustic measurements. *Journal of Asian Earth Sciences*, *57*,
475 128–136.
- 476 Wang, R., Parolai, S., Ge, M., Jin, M., Walter, T. R., & Zschau, J. (2013). The 2011
477 M_w 9.0 Tohoku earthquake: Comparison of GPS and strong-motion data. *Bul-*
478 *letin of the Seismological Society of America*, *103*(2B), 1336–1347.
- 479 Wei, S., Graves, R., Helmberger, D., Avouac, J.-P., & Jiang, J. (2012). Sources of
480 shaking and flooding during the Tohoku-Oki earthquake: A mixture of rupture
481 styles. *Earth and Planetary Science Letters*, *333*, 91–100.
- 482 Xie, Z., & Cai, Y. (2018). Inverse method for static stress drop and application
483 to the 2011 M_w 9. 0 Tohoku-Oki earthquake. *Journal of Geophysical Research:*
484 *Solid Earth*, *123*(4), 2871–2884.
- 485 Yagi, Y., & Fukahata, Y. (2011). Rupture process of the 2011 Tohoku-Oki earth-
486 quake and absolute elastic strain release. *Geophysical Research Letters*,
487 *38*(19).
- 488 Yamazaki, Y., Cheung, K. F., & Lay, T. (2018). A self-consistent fault slip model for
489 the 2011 Tohoku earthquake and tsunami. *Journal of Geophysical Research:*
490 *Solid Earth*, *123*(2), 1435–1458.
- 491 Yokota, Y., Koketsu, K., Fujii, Y., Satake, K., Sakai, S., Shinohara, M., &
492 Kanazawa, T. (2011). Joint inversion of strong motion, teleseismic, geodetic,
493 and tsunami datasets for the rupture process of the 2011 Tohoku earthquake.
494 *Geophysical Research Letters*, *38*(7).

- 495 Yue, H., & Lay, T. (2013). Source rupture models for the M_w 9.0 2011 Tohoku
496 earthquake from joint inversions of high-rate geodetic and seismic data. *Bul-*
497 *letin of the Seismological Society of America*, *103*(2B), 1242–1255.
- 498 Zhou, X., Cambiotti, G., Sun, W., & Sabadini, R. (2014). The coseismic slip dis-
499 tribution of a shallow subduction fault constrained by prior information: the
500 example of 2011 Tohoku (M_w 9.0) megathrust earthquake. *Geophysical Jour-*
501 *nal International*, *199*(2), 981–995.